Theoretical and Applied Climatology (2025) 156:238
https://doi.org/10.1007/s00704-025-05454-7

RESEARCH

Evaluation of Vertically Integrated Liquid water content using polarimetric Doppler Weather Radar

Albin Sabu[1] · Hamid Ali Syed[2] · Gargi Rakshit[3] · Someshwar Das[1,4] · S.K. Panda[1] · Devesh Sharma[1] · Jayanti Pal[1]

Received: 25 September 2024 / Accepted: 21 March 2025

Abstract
Accurate evaluation of cloud microphysical variables is essential for improving cloud parameterization and weather forecasting, yet obtaining high-resolution, spatially and temporally extensive data remains a challenge due to the limitations of in-situ measurements. The present study tries to address this gap by assessing existing equations for estimating vertically integrated liquid water content (VIL, kg/m^2) from liquid water content (LWC, g/m^3) using C-band dual-polarized Doppler Weather Radar (DWR) data from the India Meteorological Department (IMD) Jaipur station over 78 summer monsoon days in 2020–2022. A long-term climatological analysis (2003–2023) of total column cloud liquid water (TCCLW, kg/m^2) from ERA5, liquid water cloud water content (LWCP, kg/m^2) from MODIS, and rainfall data from IMD, IMERG, and GPCP datasets has been performed. VIL is computed as the vertical integral of LWC across atmospheric layers using four reflectivity-LWC (Z-LWC) relationships and one reflectivity-differential reflectivity (Z, ZDR-LWC) relationship from existing literature. The performance of empirically radar derived VIL has been evaluated by comparing with satellite-derived (MODIS) cloud liquid water path (LWP, kg/m^2) and TCCLW. The results show that VIL values increase with rainfall intensity, leading to higher estimation errors. Among all relations tested, the hybrid equation (which includes Z and ZDR) consistently demonstrated superior performance, particularly during high-intensity rainfall events, with lower root mean square error (RMSE) and mean absolute error (MAE) values. The method also captured more detailed spatial patterns of liquid water distribution with reduced bias, making it the most reliable estimator. Despite limitations such as beam blockage and slight spatial shifts due to interpolation, the current study may provide a foundation for improving real-time precipitation forecasts and understanding cloud microphysics by incorporating polarimetric radar products. The future work may aim at refining the methodology through enhanced cloud-type-specific estimators.

1 Introduction

Clouds significantly impact various aspects of the Earth system such as solar radiation, energy fluxes, the hydrological cycle, and freshwater distribution, and their study is crucial for modern meteorology and weather forecasting (Stephens et al. 2015; Pinsky and Khain 2018). The way cloud microphysical processes are represented in cloud parameterization schemes can greatly affect cloud-climate feedback in global climate models (Bodas-Salcedo et al. 2019). As clearly stated by Randall et al. (2003), cloud microphysics represents one important part of the broader cloud parameterization challenge, which has been called "a problem that refuses to die." While understanding the clouds and their processes, one of the key factors of interest is vertically integrated liquid water content (VIL), typically measured in kg/m^2. VIL is a measure of the total amount of liquid water contained in clouds within a column of the atmosphere extending from the ground to the top of the cloud layer, which determines the distribution and amount of liquid water in clouds (Liou and Ou 1989; Seo et al. 2020).

VIL has proven to be a highly useful parameter in various aspects of meteorology, such as severe thunderstorm warnings regardless of air mass characteristics and geographic location, radar-rainfall estimation, effective identification of

✉ Jayanti Pal
jayanti.pal@curaj.ac.in

[1] Department of Atmospheric Science, Central University of Rajasthan, Ajmer, RJ, India

[2] Department of Earth, Atmospheric, and Planetary Sciences, Purdue University, West Lafayette, IN, USA

[3] India Meteorological Department, Ministry of Earth Sciences, Government of India, New Delhi 110003, India

[4] Present Address: South Asian Meteorological Association (SAMA), New Delhi, India

hailstorms and estimating errors in artificial precipitation suppression operations, and providing detailed information on convective precipitation bands, aiding in nowcasting and predicting precipitation development and movement (Amburn and Wolf 1997; Witt et al. 1998; Seo et al. 2020; Islam and Rasmussen 2008; Skripniková and Řezáčová 2014). VIL also helps in tackling the challenge of classification of precipitation types beneficial to meteorology research and weather forecasting (Yang et al. 2013, 2019). Furthermore, integrating VIL data into numerical models shows promising results. Georgakakos (2000) created a method to improve rain forecasts by assimilating VIL data from weather radar and surface rainfall measurements in weather models. The above study shows a substantial reduction in the model-predicted state variance for the grid column with observations. Recently, Lai et al. (2020) proposed a scheme for getting pseudo water vapor (qv) and pseudo-potential temperature (θ) observations based on VIL, whose assimilation into the Weather Research and Forecasting (WRF) model resulted in improved composite reflectivity and precipitation forecasts. VIL, derived from X-band polarimetric weather, can also be used to predict rainfall amounts using a combination of Z and differential phase (KDP) (Hirano and Maki 2010). These ongoing studies highlight the need for a more in-depth examination of this parameter at a regional scale.

VIL is typically derived from the vertical integration of radar reflectivity observations (Greene and Clark 1972). Matrosov (2009) estimated the vertical integral of cloud ice, liquid, and mean rain rate in stratiform precipitation with lesser uncertainties, where radar and auxiliary data including a ground-based disdrometer were used. According to Li et al. (2015), cloud water content profile in warm rains can be well determined by cloud water path (CWP), cloud top height (CTH), and cloud bottom height (CBH). Algorithms utilizing these parameters demonstrated good performance in WRF-ARW model simulations. Gascón et al. (2015) analysed a convective winter event over the Iberian Peninsula using a multichannel microwave radiometer and retrieved the vertical profile of LWC by determining cloud boundaries from thermodynamic profiles using a theoretical cloud model. Lyras et al. (2017) proposed a stochastic dynamic model for the generation of VIL fields to predict the impact of cloud impairments on satellite links. Zheng et al. (2019) employed a method that uses both X-band rain radar and Ka-band cloud radar together in vertical detection mode to estimate VIL. This approach, unlike traditional methods that use volume scan data, improved the accuracy of VIL calculations. When compared with Global Precipitation Measurement (GPM) data, their method showed better results in estimating VIL. Seo et al. (2020) used radar reflectivity data and temperature sounding from an atmospheric sounding to construct a polar-based reference map of reflectivity that contains reflectivity observations below the melting layer to estimate VIL, which helped to reduce bright band (BB) effects in quantitative precipitation estimation (QPE). Schulte et al. (2024) used a random forest algorithm to predict cloud LWC from combined CloudSat/CALIPSO observations; their study observed a daytime oceanic warm cloud liquid increase of about five-fold compared to observation. Even though different estimation methods exist, the primary challenges in estimating VIL primarily stem from a lack of continuous and global observations. Studies using microwave radiometers and disdrometers benefit from scientific understanding but are limited by high costs, complexity, and restricted spatial coverage, reducing their impact on operational forecasting (Saunders 2018; Tapiador et al. 2017; Angulo-Martínez et al. 2018). The challenges of collecting continuous data from aircraft arise from the cost and limited duration of observations (Aydin and Singh 2004; Yum et al. 2004). Zhong et al. (2011) discussed the limitations of meteorological satellites and ceilometers in observing the 3D shape of clouds and identifying their internal characteristics since they primarily direct the upper and lower boundaries of the cloud.

Bulk microphysics schemes (BMSs) are commonly adopted in NWP models and are essential for accurate forecasting of precipitation, cyclone track, and intensity. (Fovell and Su 2007; Pattnaik et al. 2011). Yang et al. (2024) assimilated radar reflectivity using a full-hydrometeor scheme with WSM6 in WRF 4D-Var, showing improved model spin-up and enhanced 0–3 h accumulated precipitation forecasts. Wang et al. (2024) demonstrated that directly assimilating radar reflectivity using a two-moment microphysics scheme effectively adjusted hydrometeors and large-scale variables, particularly temperature and vertical velocity, in a typhoon landfall study in China. In a developing country like India, ground measurement of precipitation hydrometeors like rain, snow, or hail are not only challenging but also costly. However, effective use of 3D observations from DWR can provide valuable insights about hydrometeors.

Widener and Mead (2004) detailed the use of W-band atmospheric radiation measurement cloud radars for high-resolution cloud data collection over long periods. Moran et al. (1998) documented the use of vertically pointing Ka-band millimetre-wave cloud radars for collecting cloud data. Integrating radar and satellite data is crucial for regional precipitation forecasting due to their high resolution and extensive coverage. Radar, sensitive to higher moments of the drop size distribution (DSD), and satellites, capturing lower moments, together offer essential microphysical insights for accurate BMS evaluation. Mohan et al. (2024) evaluated WRF cloud microphysics schemes for tropical cyclone Fani using wind profiler radar and multi-satellite data, finding that scheme variations mainly influenced intensity while having a lesser impact on track predictions. Roh et al. (2024) evaluated a global non-hydrostatic model over Japan using a ground-based Cloud Profiling Radar similar to EarthCARE's, assessing microphysics schemes via Doppler velocity. Results highlight the significant impact of microphysics choice on hydrometeor phase separation and terminal velocities.

Therefore, the present study utilizes the dual-polarimetric DWR together with satellite and reanalysis datasets for cloud microphysical parameter estimation. This enables the effective use of dual- polarimetric and base products of the DWR. The primary aim of the study is to understand the capability of existing empirical equations in retrieving VIL from DWR using LWC equations. This has been estimated using variables such as ZDR and reflectivity. Various empirical relationships for estimating LWC using these variables are discussed in subsequent sections. Each relationship is applied to calculate VIL and evaluated through qualitative and quantitative analysis; subsequently, the best among existing methods has been identified for further examination in future work. The present study is the first of its kind over the Indian domain.

The study is organized into different sections. Section 2 includes an explanation of the data and methodology used in this work and provides an overview of the various equations employed. Section 3 discusses the long-term analysis of total column cloud liquid water (kg/m^2) (hereafter TCCLW) and liquid water cloud water path (kg/m^2) (hereafter LWCP) along with different sets of rainfall data, and qualitative and quantitative evaluation of retrieved VIL from each equation is added. Finally, in Section 4, a brief overview of the study is given along with a discussion of the major outcomes.

2 Data and methodology

2.1 Data

The present study focuses on the evaluation of existing VIL estimation relations for the selected days of the summer monsoon (hereafter SM) season, June, July, August, and September (hereafter JJAS) for the years 2020, 2021, and 2022. To achieve the research objective, DWR data, reanalysis data, satellite data and gridded rainfall have been used.

2.1.1 Doppler Weather Radar

This study utilized DWR data from the IMD, Jaipur (26.8207°N, 75.8157°E), which is a C-band dual polarimetric DWR. The IMD typically collects radar data using two different coverage patterns. The first is long-range PPIs, referred to as Type-C (500 km radius), which usually consists of 1 to 3 sweeps. The second is short-range PPIs, known as Type-B, which includes 5 to 10 different sweeps. In this study, we utilized the Type-B (250 km radius) pattern radar data, which has 10 different sweeps taken at 10 different elevation angles, 360 rays (1° resolution of azimuths) and 999 gates per sweep. Being an operational radar, it was calibrated for system gain and incorporated noise level corrections and offset adjustments to rectify imbalances in the receiver channels. To enhance data quality, signal thresholds were applied to eliminate clutter and weak signals, while a statistical calibration fit ensured measurement consistency (George et al. 2011). Additionally, sun calibration, frequency adjustments, and transmitted power corrections were implemented (Rinehart 2004). Thus, the radar appears well-calibrated. To keep biases in quantitative precipitation estimates under 20%, a sensitivity of 0.1–0.2 dB for ZDR and ± 1 dB to ± 2 dB for Z is expected from an operational radar, making the uncertainty in the VIL measurements least (Seliga and Bringi 1976; Bringi and Chandrasekar 2001; Frech and Hubbert 2020). We use reflectivity (Z, dBZ) and differential reflectivity (ZDR, dB) for the study. Reflectivity refers to the measure of the amount of transmitted radar signal that is reflected to the radar receiver by scatterers. ZDR is the logarithmic ratio between the backscattered power at horizontal and vertical polarizations, which is close to 0 dB for isotropic scatterers and shows larger positive values for oblate particles. The specifications of radar and details of radar data are given in Table 1.

2.1.2 ERA5 data

Data from the Reanalysis 5th Generation dataset (ERA5) (Hersbach et al. 2020) of the European Centre for Medium-Range Weather Forecast (ECMWF), which includes a comprehensive record of the global atmosphere, land surface, and ocean waves from 1950 onward with global coverage at hourly and monthly time scales, is used to analyse

Table 1 Specification and details of IMD Jaipur Doppler Weather Radar and corresponding DWR data

Conventions	CF/Radial
Coordinates	Polar
Number of sweeps	10
Scan types	B and C
Wavelength	5 cm
Frequency	5625 MHz
Altitude	399 m from sea level
Range	250 km
Sweep angles (°)	0.5, 1, 2, 3, 4.5, 6, 9, 12, 16, 21
Variables available	Reflectivity (dBZ) Radial Velocity (m/s) Spectrum Width(m/s) Differential Reflectivity (dB) Echo classification (Unitless)
Data format	NetCDF

the climatology and assess the retrieved VIL. The spatial resolution of the hourly single-level TCCLW (kg/m^2) is $0.25° \times 0.25°$. The amount of liquid water in cloud droplets across a column that runs from the Earth's surface to the top of the atmosphere is represented by this parameter. It is based on a global reanalysis model that represents liquid water as an area-averaged value over a model grid box, simplifying cloud microphysics. Additionally, ERA5 hourly precipitation type data, which describes the type of precipitation with a spatial precision of $0.25° \times 0.25°$, is used for additional analysis.

2.1.3 MODIS datasets

This study has made use of three distinct sets of Moderate Resolution Imaging Spectroradiometer (MODIS) data. The Afternoon Constellation (A-train) of the MODIS on board the Aqua and Terra satellites provided the satellite observations used in this investigation (Platnick et al. 2017). Cloud water path (kg/m^2) and cloud phase have been taken from MODIS available at a spatial resolution of 1 km. These data were obtained from the collection 6.1, level 2 Atmosphere, Land (ArchiveSet 61) data product. On one of the chosen days (June 25, 2020), when the MODIS swath and the entire radar sector overlapped, this MODIS data was taken into consideration. This was carried out to illustrate the procedures followed in this investigation. This choice was made in an effort to balance radar data accessibility.

The long-term average is examined using the gridded LWCP (kg/m^2) from the MODIS Aqua and Terra satellites for the years 2003–2023 that were acquired via the Geospatial Interactive Online Visualization ANd aNalysis Infrastructure (GIOVANNI).

2.1.4 Rainfall datasets

Present study includes rainfall data from three different sources at different spatial resolution, which have been utilized for long-term spatial analysis. With 135 longitude locations (66.5E to 100.0E) and 129 latitude points (6.5N to 38.5N), the IMD's new high spatial resolution ($0.25° \times 0.25°$) long period (1901–2022) Daily Gridded Rainfall Data Set (Pai et al. 2014) covers the entire landmass of India. Another multi-satellite merged high resolution rainfall product (Huffman et al. 2014), IMERG (Integrated Multi-satellitE Retrievals for Global Precipitation Measurement) provides daily global rainfall at 10 km. Additionally, the $1° \times 1°$ spatial resolution GPCP (Global Precipitation Climatology Project) Monthly Analysis Product (Adler et al. 2003) was used, which combined data from several satellite sources covering both land and ocean and was augmented by gauge observations over land areas.

2.2 Methodology

The PyScanCf (Syed et al. 2024) Python package has been used for processing IMD weather radar data. The first step is to integrate the obtained multi-sweep radar data into conventional polar volumes. Numerous pollutants, primarily from biological and ground clutter, can affect the DWR data. The remaining ground clutter was eliminated using the Gabella clutter filter (Gabella and Notarpietro 2002), a successful two-part identification algorithm based on texture analysis that uses minimum echo area and echo continuity criteria to distinguish between meteorological and non-meteorological echoes. Additionally, radar data was corrected for attenuation gate-by-gate using the iterative method suggested by Jacobi and Heistermann (2016) and Kraemer and Verworn (2008).

The Python module Wradlib contains these algorithms (Heistermann et al. 2013). Additionally, PyART (Helmus and Collis 2016), an open-source Python library made specifically for working with weather radar data, is used to transform the analyzed CfRadial files to gridded format. Gridding was done using the adaptive Barnes scheme (Barnes 1964), an interpolation scheme in which values at grid points are estimated using a weighted average technique depending on the distances to surrounding radar data points. The radar data is gridded to a spatial resolution of 2 km and 40 levels vertically up to 20 km height, providing 500 m of vertical spacing. The processing of radar data has been depicted in a flow diagram, displayed in Fig. 1. A long-term time average spatial analysis of the TCCLW and LWCP datasets was then conducted in conjunction with rainfall data to obtain a better understanding of the spatial characteristics of liquid water content over the study domain during SM from 2003 to 2023. Events were chosen for the present study based on three criteria: days with area-weighted average rainfall of at least 8.3 mm, days with area-weighted average rainfall exceeding 62.5 mm, and more than 50% of the grid showing rainfall over 2.5 mm within the 250 km radius domain of IMD Jaipur radar range. In this study, 78 similar instances that met these criteria were examined. Out of 78 days, 18 are from 2020, 28 are from 2021, and 38 are from 2022 during SM months. Table 2 lists the available radar data.

2.2.1 VIL estimation

To estimate VIL the process begins by filtering out radar reflectivity values less than 20 dBZ. This threshold was selected based on initial observations of persistent clutter and insights from previous studies, which indicate that non-meteorological echoes typically fall below this value (Nesbitt et al. 2006 and Cifelli et al. 2007). Further, the maximum height to which the system was extended was identified using maximum reflectivity (MaxZ) analysis, which display the vertical height, cross section and maximum reflectivity

Fig. 1 Flow chart of IMD-Jaipur DWR data pre-processing

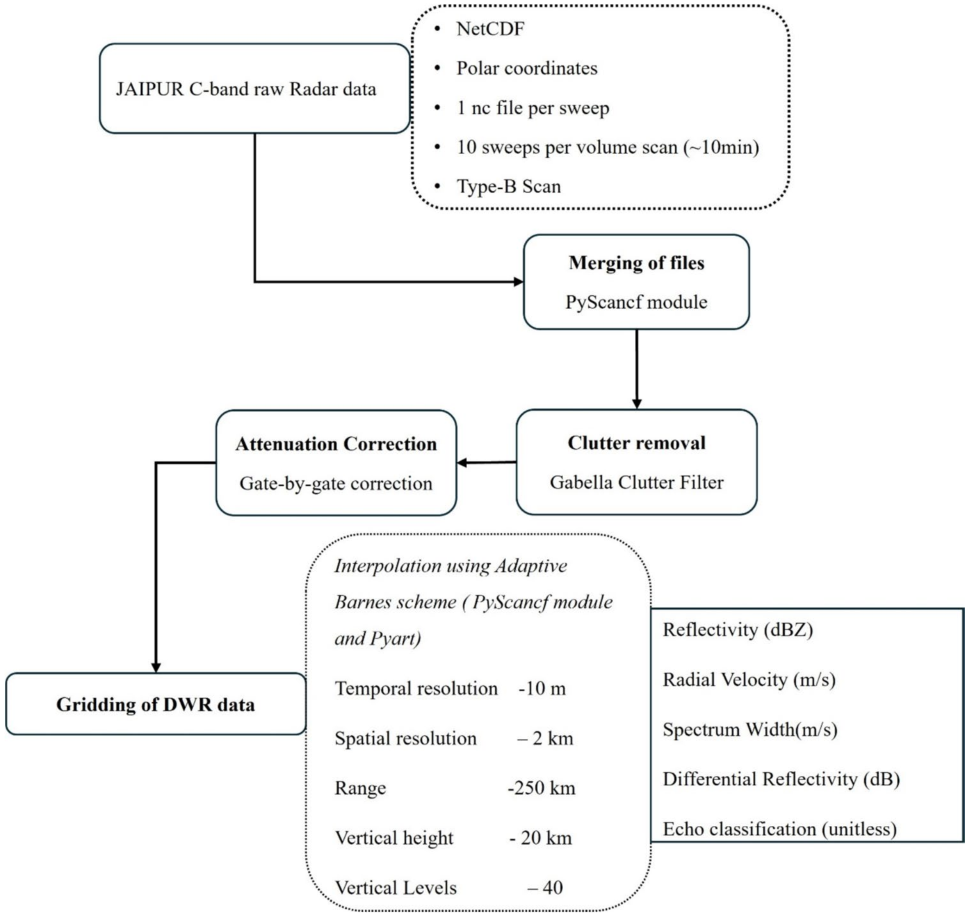

Table 2 DWR data received from IMD for summer monsoon period (JJAS) for the years 2020, 2021 and 2022

Year	Fraction missing data (%)	Longest outage (days)
2020	47.66	36
2021	19.65	2
2022	33.55	13

Table 3 List of Empirical formula used to estimate LWC from DWR

Equation Number	
2.1	$\log(LWC(Z)) = 0.057Z - 2.46$
2.2	$\log(LWC(Z)) = 0.066Z - 2.80$
2.3	$\log(LWC(Z)) = 0.050Z - 2.18$
2.4	$\log(LWC(Z)) = -0.0005Z^2 + 0.084Z - 2.77$
2.5	$\log(LWC(Z, ZDR)) = 0.058Z - 0.118ZDR - 2.36$

from all levels (refer Fig. 8b for an example of MaxZ plot). This height corresponds to the number of levels used in the integration at each time. Five sets of LWC equations were used in this study, refer to Table 3. Proposed by Greene and Clark (1972), Eq. 2.1 establishes a linear relationship between the logarithm of LWC and horizontal radar reflectivity. Carlin et al. (2016) introduced Eq. 2.2 as an alternative linear model for estimating LWC from Z, reflecting slight variations in empirical coefficients derived from German DSDs and Eq. 2.3 is linear and Eq. 2.4 is the quadratic fit of the same. These equations are Z- LWC based equations where Eq. 2.5 is the bivariate linear estimator introduced by Carlin et al. (2016) which provides a method to estimate LWC using Z and ZDR.

For uniformly spaced vertical levels at 500 m intervals, the calculation of VIL involves summing the LWC values at each level and then multiplying by the vertical height interval using Eq. 1. This method ensures an accurate representation of the total liquid water content per unit area, fully accounting for the vertical extent of the cloud column.

$$VIL = \sum_{i=1}^{n} LWC_i . \nabla h \tag{1}$$

where i is the number of levels, LWC is the liquid water content of each level and h is the thickness of each vertical layer. VIL is first computed for each hour and then converted to daily by averaging the hourly data. Figure 2 shows a flow diagram for VIL computation and analysis. To assess the quality of the estimators, several metrics are utilised. The Pearson Correlation Coefficient (r) gauges the strength and direction of linear relationships between variables, Mean Absolute Error (MAE) quantifies the average magnitude of prediction errors, offering a measure of overall accuracy, Root Mean Squared Error (RMSE) provides a standardised measure of these errors, giving more weight to larger deviations, Standard deviation (STD) reflects how much individual data points differ from the mean, highlighting the variability within the dataset, Mean Bias Deviation (MBD) reveals the average bias in predictions, indicating how much predicted values deviate from observed values and finally, Bivariate Moran's I (BMI) evaluates the spatial correlation between observed and retrieved values, uncovering spatial patterns that are crucial for understanding regional dependencies (Lee 2001) were employed.

3 Results and discussions

3.1 Long-term average of LWCP and TCCLW during the summer monsoon months of the years 2003 to 2023

The spatial distribution of average LWCP and average TCCLW for the SM months of the years 2003 to 2023 is given in Fig. 3a and b, respectively. This section provides an overview of LWCP and TCCLW over the domain, as this is the first study of its kind in this region. The goal is to acquaint readers with the range and spatial distribution of these variables before proceeding with the estimation process. The LWCP has a higher value ranging more than 0.07 kg/m^2 in the south and southeastern part and the trend decreases towards the western and northwestern part of the region making an approximate diagonal spatial pattern of lower value on the left and higher on the right. TCCLW also shows a similar diagonal spatial pattern with values ranging from 0.1 to 0.14 kg/m^2 in the south and southwestern part of the region with a much higher value than 0.14 kg/m^2 in between 76.5°E and 77.5°E, the southeastern part adjoining and including Madhya Pradesh (MP). The averaged rainfall pattern of JJAS for the same year range from IMD gridded, IMERG and GPCP is shown in Fig. 4a, b and c respectively. This also shows a northeastward diagonal decrease as same as the TCCLW and LWCP. The much higher value of rainfall (> 8 mm/day) is seen in the southeastern region of the range, that is the region adjoining the neighboring state of MP. These are the regions with higher values of LWCP and TCCLW are observed.

To gain a deeper understanding of spatial patterns of the monthly variations, LWCP and TCCLW alongside average rainfall during the SM months are studied. In June the LWCP values are generally below 0.15 kg/m^2 (Fig. 5a). Only the central part and southeastern part show the values more than this. TCCLW in June (Fig. 6a) shows an overall value of less than 0.13 kg/m^2 with slightly higher in the southeastern region.

Fig. 2 A flow diagram for VIL computation and analysis

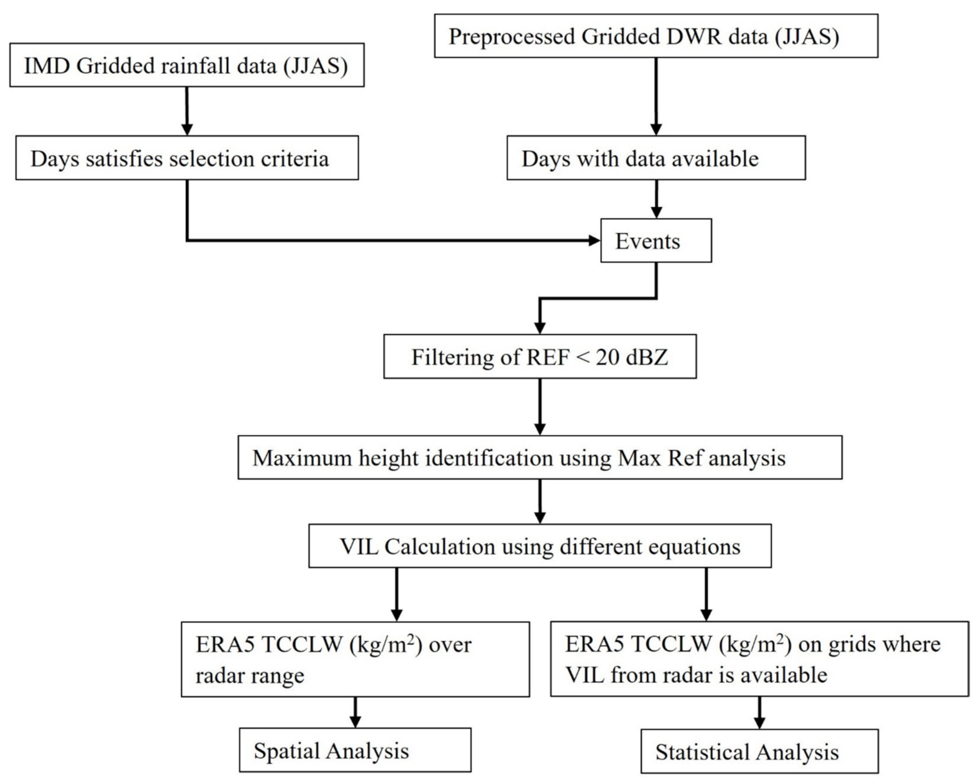

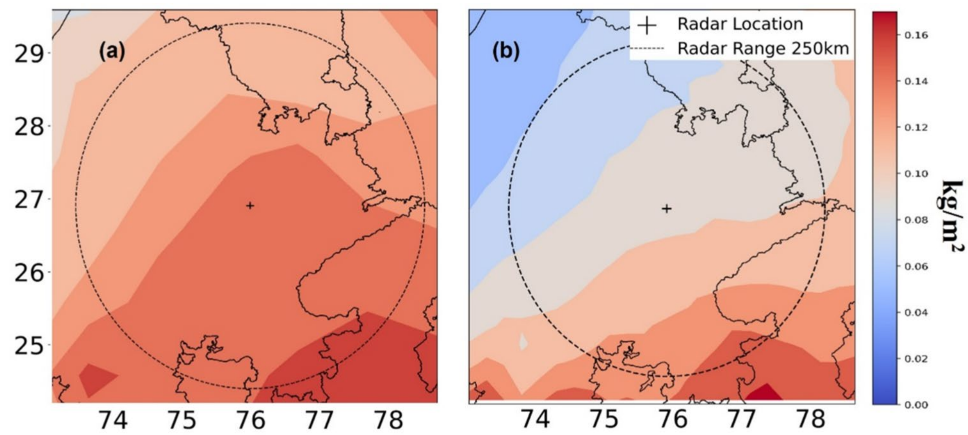

Fig. 3 (**a**) Average LWCP (kg/m^2) from MODIS (**b**) Average TCCLW (kg/m^2) from ERA 5 during JJAS for the period of 2003–2023 over a region centering at DWR-Jaipur location (24N-30N; 73E-79E)

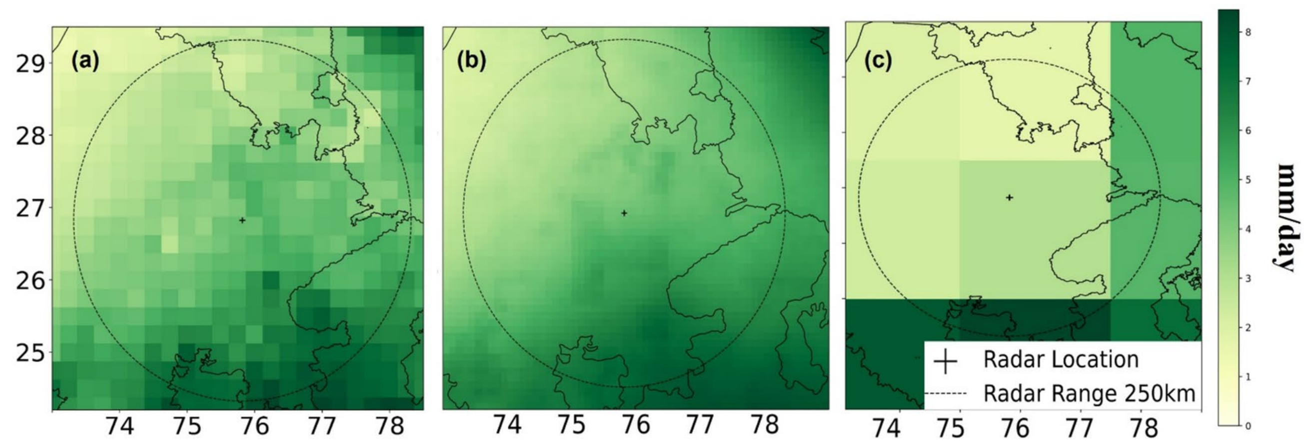

Fig. 4 Average Rainfall (mm/day) from (**a**) IMD gridded (**b**) IMERG and (**c**) GPCP during JJAS for the period of 2003–2023 over a region centering at DWR-Jaipur location (24N-30N; 73E-79E)

Rainfall during June (Fig. 7a, b, c) shows a higher value in the southeastern part where the LWCP and TCCLW are also high. This aligns with the timing of the SM's arrival in the area which occurs by the end of June and is fully established by July (Ali et al. 2005) where it progresses from the southeastern part of the state. In July (Fig. 5b), the LWCP plots show that most of the region has values exceeding 0.18 kg/m^2 whereas the northwestern part has very less value compared to other regions. TCCLW in July (Fig. 6b) has a maximum value of more than 0.24 kg/m^2 in the southeastern part and the northwestern part has a lower value. From the rainfall plot of July (Fig. 7d, e, f) it is observed that rain has covered most of the region with rainfall of more than 6 mm/day except the northwestern part where the LWCP and TCCLW are also less. A similar trend is observed for LWCP and TCCLW in August also (Figs. 5c and 6c respectively) with the south and southeastern parts having higher values. LWCP values in the south and central parts have increased to more than 0.21 kg/m^2. Rainfall over this region also increased during this month (Fig. 7g, h, i). LWCP and TCCLW is decreased in September (Figs. 5d and 6d respectively) as the rainfall decreases and retreats during this month (Fig. 7j, k, l). The central and northwestern parts have LWCP and TCCLW values less than 0.15 kg/m^2. Rainfall has also been reduced to less than 6 mm/day in those regions. The northwestern part still has less rainfall and less LWCP and TCCLW in this month as well.

LWCP and TCCLW during the SM months show a clear pattern of higher values in the south and southeastern part in the months of July and August which are the months when the rainfall reaches, peaks and covers the entire state. While in the months of June and September the values are lower in the north and northwestern part of the region and comparatively higher in the south and southeastern making diagonal variation visible. These lower and higher values correspond to the early days of arrival and withdrawal timings of the SM. Deep convective and nimbostratus clouds being dominant during the southwest monsoon and western disturbances (Johansson et al. 2015; Kumar et al. 2019), these thicker clouds result in larger cloud liquid water and rain liquid water, causing greater rain rate during the monsoon in China (Zhang et al. 2020). These deep convective clouds are characterized by extensive vertical heights, reaching up to

Fig. 5 Monthly average LWCP (kg/m^2) from MODIS for (**a**) June (**b**) July (**c**) August and (**d**) September for the period of 2003 – 2023 over a region centering at DWR-Jaipur location (24N-30N; 73E-79E)

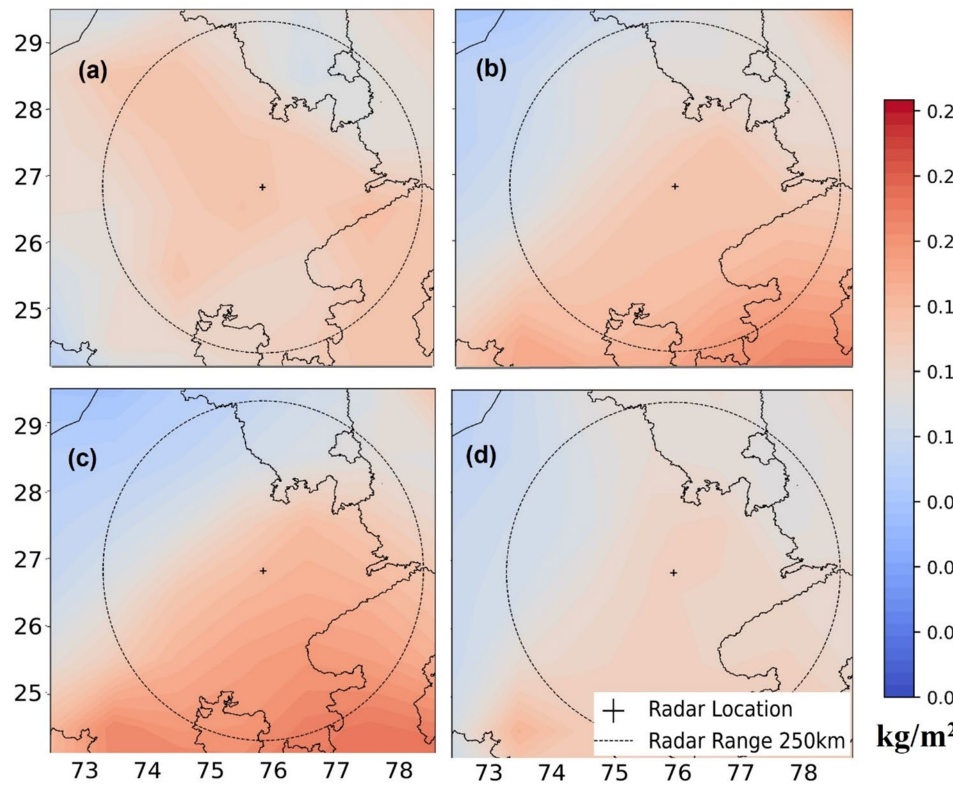

Fig. 6 Monthly average TCCLW (kg/m^2) from ERA 5 on (**a**) June (**b**) July (**c**) August and (**d**) September for the period 2003–2023 over a region centering at DWR-Jaipur location (24N-30N; 73E-79E)

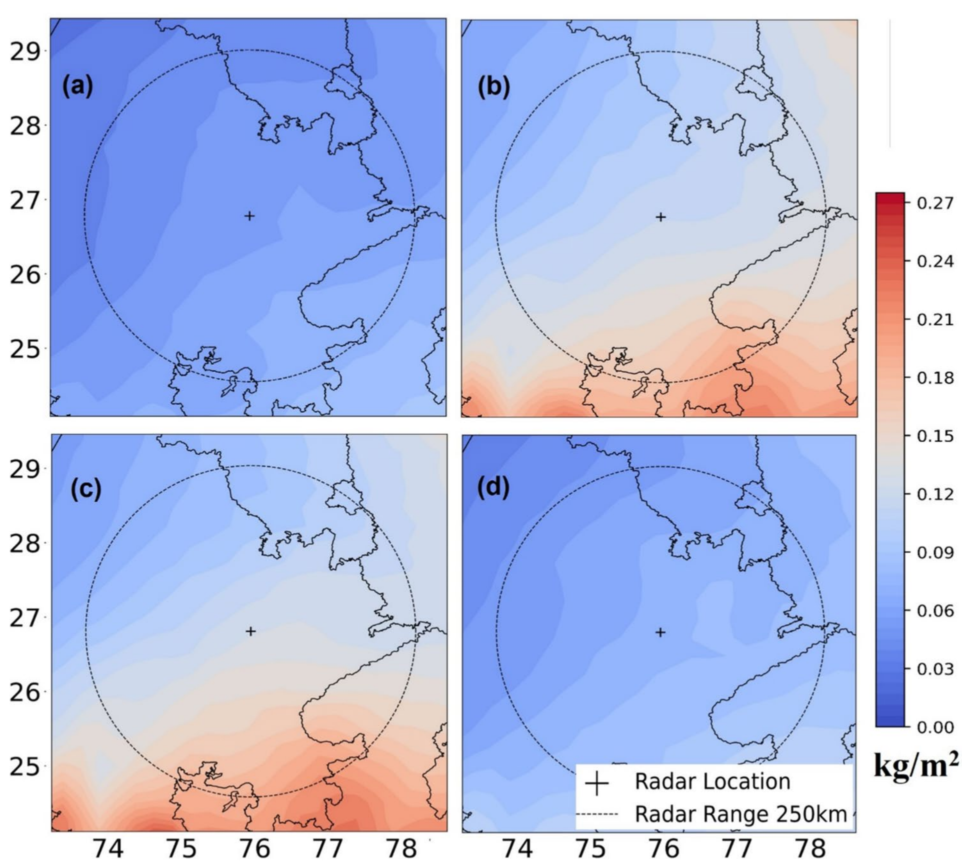

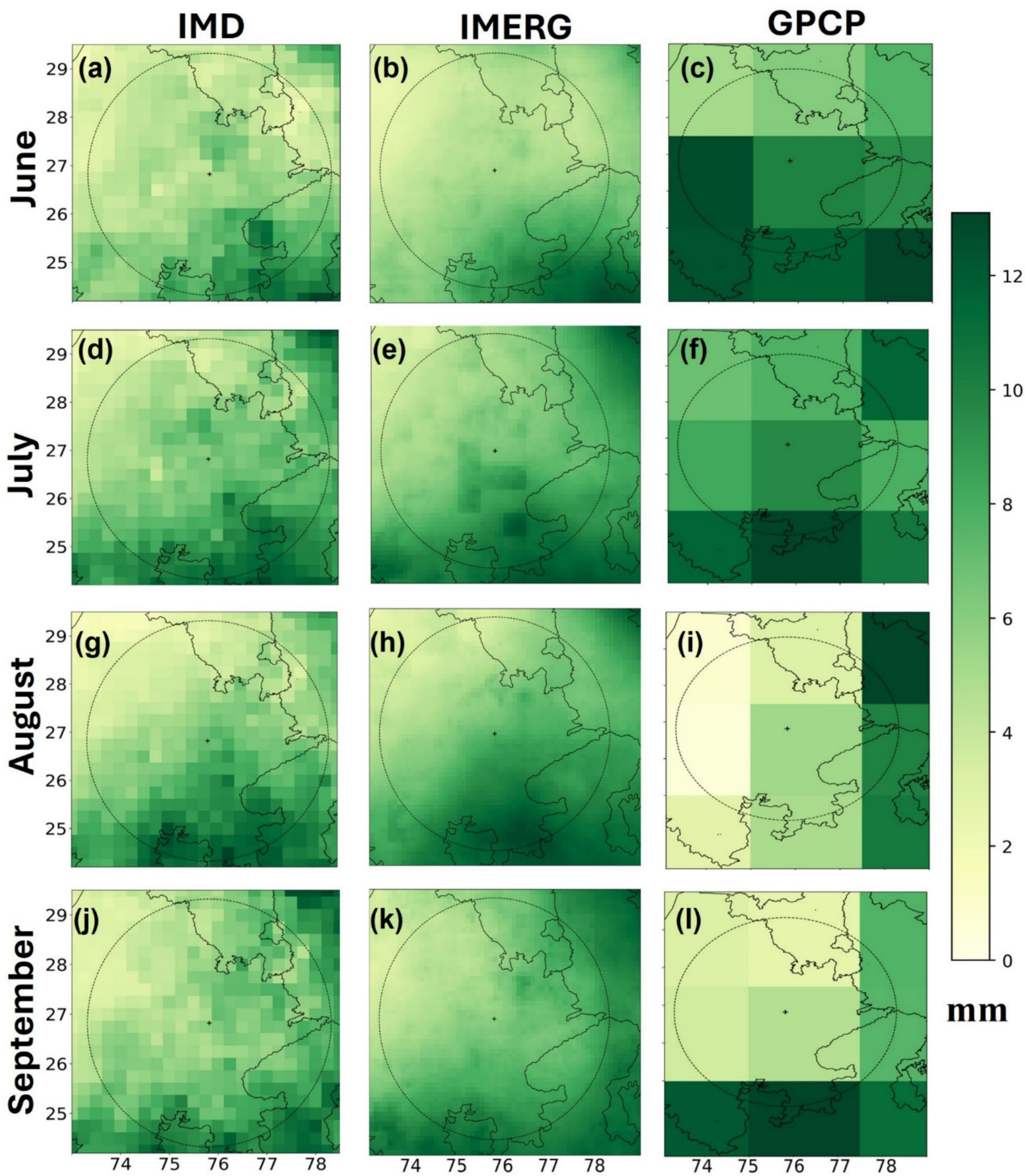

Fig. 7 Monthly average rainfall(mm) for from IMD gridded, IMERGE and GPCP over Jaipur radar range during June (**a-c**), July (**d-f**), August (**g-i**), September (**j-l**) respectively for the period 2003 to 2023 over a region centering at DWR-Jaipur location (24N-30N; 73E-79E)

14 km, and significant cloud water and ice content (Rajeevan et al. 2013). This could be the reason for elevated values of LWCP and TCCLW during the months of July and August. The increase in LWCP and TCCLW in the diagonal region is likely due to enhanced cloud formation caused by orographic lifting over the Aravalli Range, which is the dominant mountain range in Rajasthan that roughly divides the state into two halves diagonally (Roy and Jakhar 2002).

3.2 Evaluation of LWC equations

To begin the evaluation, we will first analyse the VIL for 25 June 2020, focusing particularly on the mature stage hour of the system (13:00 UTC), where each equation will undergo detailed analysis. Then, the analysis is conducted for the entire day and is validated against observations and other parameters. After that, the detailed statistical analysis of VIL for all other selected days (daily analysis) is carried out. VIL is compared with TCCLW, both of which quantify the total liquid water content in cloud droplets across a vertical column from the Earth's surface to the top of the atmosphere, measured in kg/m^2.

3.2.1 During mature stage

The synoptic conditions during the mature stage of the system on 25 June 2020 13:00 UTC were studied and VIL was estimated and analysed for this hour. On 25 June 2020, the Jaipur radar region witnessed a system of convective rain-bearing clouds leading to widespread rainfall and destruction, with 13:00 UTC marking the hour when the system matured. The INSAT-3D satellite brightness temperature (K) (Fig. 8a), radar reflectivity plots of maximum reflectivity (dBZ) (Fig. 8b), 24 h total accumulated rainfall (Fig. 8c) and evolution of reflectivity during the maturing and mature stage of the event (Fig. 9), were examined to assess the synoptic condition of the event.

From Fig. 8a the cloud top brightness temperature (K) for 12 15 UTC during the maturing stage shows values of 200 K or lower in all clusters of clouds including the bigger system of clouds covering Nagaur region indicating intense convection. Also, two smaller clusters over Tonk and Krauli (middle and eastern parts) which further get grouped together to form a single cell and rain show values of 200 K or lower. At the same time, the MaxZ plots (Fig. 8b) show reflectivity values higher than 30dBZ around the smaller cluster and reflectivity values more than 40dBZ inside the core of the cloud system. Vertical growth of the cloud over 15 km and some reaching up to the tropopause is seen around the core of the clouds. The core height (REF > 35dBZ) has also reached around 10 km. The same regions with maximum reflectivity received high accumulated rainfall of over 20 mm/day during the course of the day (Fig. 8c). Upon further examination of the evolution of reflectivity, it is seen that the system remains relatively stationary overall, as shown in Fig. 9. Between 11:02 UTC and 13:02 UTC, there is little development, though the structure is visible. However, starting at 13:42 UTC, the system begins to intensify. A less intense cluster with reflectivity values below 30 dBZ is observed on the left, while a smaller but more intense cloud cluster with reflectivity values exceeding 35 dBZ forms in and around the core in the southeastern part. By 14:42 UTC, the system has matured, with both structures surpassing reflectivity values of 35 dBZ, and the core reaching values of 45 dBZ or more. This situation persists for a while, and rainfall begins to subside by 16:12 UTC. Figure 10 illustrates the radar-estimated VIL retrievals across different equations with observation and bias during the mature stage. The statistical analysis is shown in Table 4.

$$\log(\mathrm{LWC}(Z)) = 0.057Z - 2.46 \tag{2.1}$$

Figure 10a represents the observed TCCLW (kg/m^2) from ERA5, and Fig. 10b shows the estimated VIL from DWR using Eq. 2.1. The overall spatial pattern of the observed and estimated VIL matches. The higher values (> 0.35 kg/m^2) in the radar-derived VIL towards the right of the observation, especially near and in the neighbouring state of MP show a good matching. However, in the observation higher values are between 75°E and 76°E longitude, whereas in the radar estimation, they are between 76.5°E and 77°E longitude. Both reanalysis smoothing and interpolation of observations could have caused the observed longitudinal displacement of extreme values in

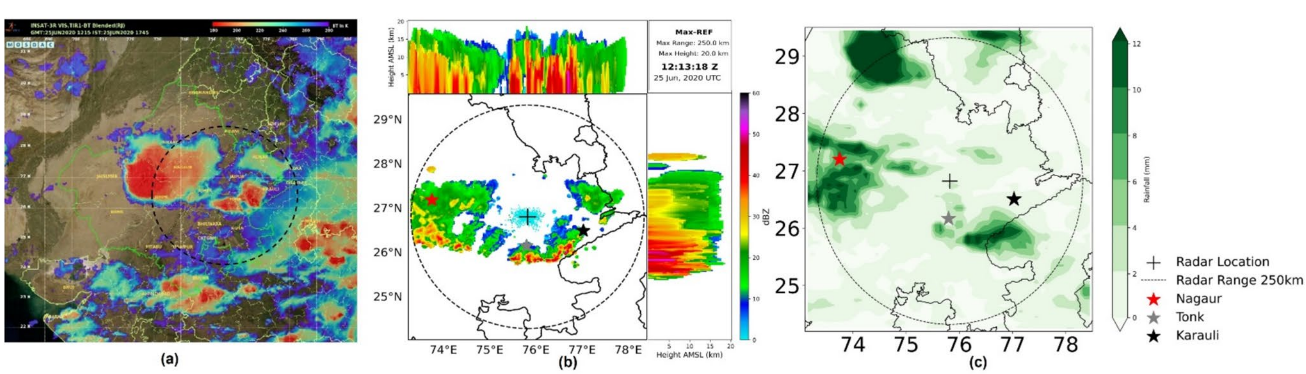

Fig. 8 Images from satellite, radar and rainfall rate on 25 June 2020, (**a**) INSAT-3D Brightness Temperature (K) at 12:15 UTC, (**b**) Jaipur IMD DWR derived maximum reflectivity (dBZ) at 12:13 UTC, (**c**) 24 h accumulated rainfall (mm)

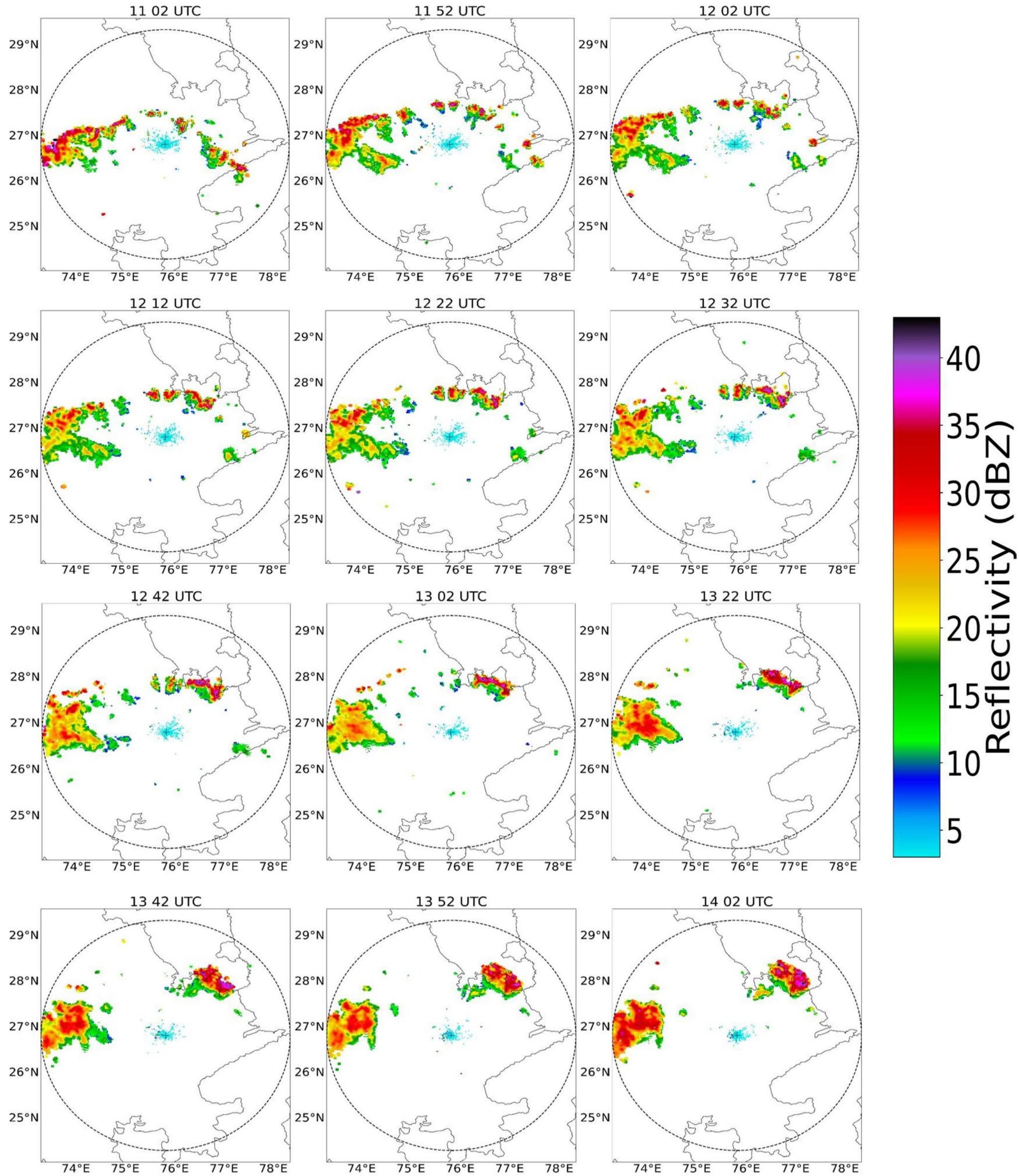

Fig. 9 Evolution of IMD gridded radar reflectivity (dBZ) during maturing stage of the event on 25 June 2020

rainfall patterns. Both observation and radar estimation show maximum values of VIL at areas where reflectivity is higher than 35 dBZ (Fig. 9). Most of the regions with lower VIL are captured by radar with an exception in regions near 27°N latitude**.** Overall bias is near zero; nevertheless, we can observe a slight overestimation in the higher VIL region (Fig. 10c). Conversely, most of the negative bias is spread in the regions of low reflectivity,

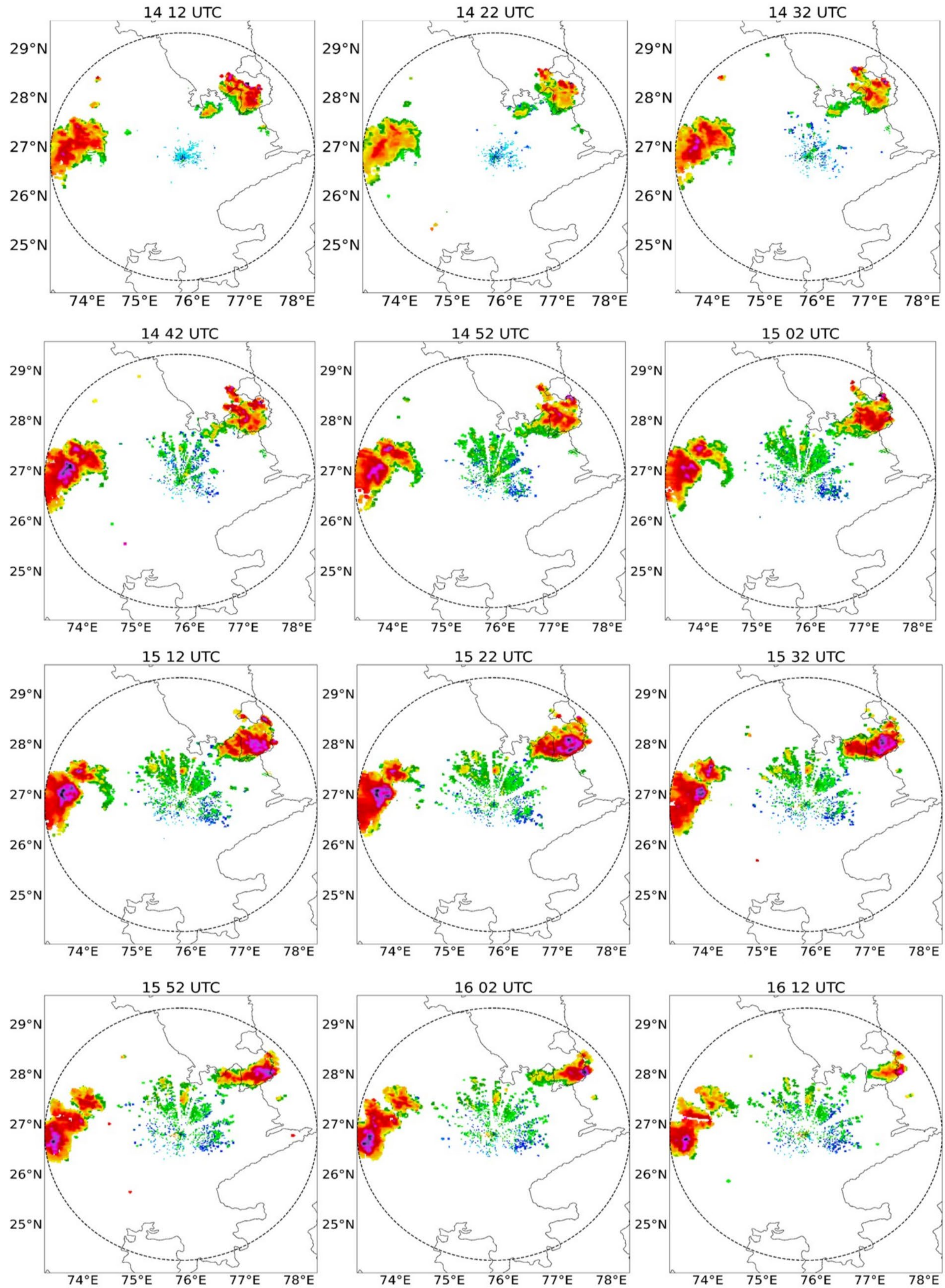

Fig. 9 (continued)

reaching below—0.3 at some regions. This negative bias may stem from factors such as attenuation effects or limitations in radar calibration near intense convective cores (Illingworth et al. 2000). VIL exhibits an STD of 0.023 which is the lowest of all, indicating moderate variability, while TCCLW shows a slightly higher STD of 0.072, suggesting greater variability. A lowest RMSD value of 0.112 during the mature stage indicates the average differences between the observed and predicted values. The MBD of −0.068 indicates an overall slight underestimation and the lowest MAE for the mature stage of 0.085 represents the average magnitude of errors. The BMI value of 0.05, with a p-value of 0.001, indicates a significant positive spatial correlation.

$$\log(LWC(Z) = 0.066Z - 2.80 \tag{2.2}$$

Comparing the radar retrieval of Eq. 2.1 with that of Eq. 2.2, the central part of the small cloud cluster around the northwestern part (28°N Latitude) becomes visible with a value of VIL more than 0.4 kg/m^2 (Fig. 10d). In comparison with observation, regions of lower VIL have been captured clearly by this equation as well. Additionally, the bias (Fig. 10e) around the high reflectivity region and the surrounding area of the larger cluster has been reduced. The bias is nearly zero with faint patches in the high reflectivity area, and the left core shows enhanced VIL values, particularly in the core region. However, in the right cluster, where the bias is reduced, the region with VIL values ranging from 0.05 to 0.1 kg/m^2 is not very visible. The spatial pattern is comparable with the observation. Equation 2.2 reveals an STD of 0.024 for VIL from radar, indicating moderate variability. The RMSD of 0.115 suggests moderate discrepancies between observed and predicted values. The MBD of −0.071 suggests a slight underestimation in VIL estimation. The MAE of 0.088 reflects the average magnitude of prediction errors, illustrating the equation's overall accuracy in estimating VIL. Moreover, the BMI of 0.5 indicates a significant spatial autocorrelation in TCCLW values, implying that nearby locations tend to have similar VIL values.

$$\log(LWC(Z) = 0.050Z - 2.18 \tag{2.3}$$

Upon analysing the Eq. 2.3 VIL retrieval (Fig. 10f), we observe better performance in capturing higher VIL values around the central region of the cluster on the western side. In the eastern cluster, the region with VIL values less than 0.5 kg/m^2 around the high reflectivity region is now visible. Additionally, the region with VIL estimated has increased in comparison with Eq. 2.1 and Eq. 2.2 in this retrieval. New regions are in lower reflectivity areas away from the central part of both clusters. These new regions are in the lower VIL range mostly showing slight underestimation with near zero negative bias (Fig. 10g). These regions can be identified in the observation as well. There is a greater positive bias in this estimation at the high reflectivity regions of both clusters compared to other equations indicating overestimation. Equation 2.3 also exhibits a lower STD of 0.027 during the mature stage. The RMSD of 0.130 has moderate discrepancies. The MBD of −0.090 suggests an underestimation in VIL predictions. The MAE of 0.103 reflects the average magnitude of prediction errors. Moreover, the BMI of 0.65 indicates a strong spatial autocorrelation between observation and estimation, implying that nearby locations tend to have highly similar values.

$$\log(LWC(Z) = -0.0005Z^2 + 0.084Z - 2.77 \tag{2.4}$$

Based on the analysis of Eq. 2.4, several distinct observations have emerged. Firstly, compared to already analysed equations, there is a noticeable reduction in the region where VIL values range from 0.05 to 0.1 kg/m^2 (Fig. 10h). Additionally, we can see a reduction in VIL estimated areas within the high reflectivity regions of the cluster in the western side, where values range from 0.1 to 0.2 kg/m^2. Moreover, a more pronounced and widespread negative bias is observed across the western cluster, which is more widespread (Fig. 10i). Equation 2.4 exhibits an STD of 0.023 for VIL from radar, indicating moderate variability. The RMSD of 0.133 is the highest among the equations. The MBD of −0.097 suggests a slight underestimation in VIL predictions. The MAE of 0.106 is the highest among all prediction errors obtained from Eqs. 2.1–2.5. Moreover, a BMI of 0.7 indicates a strong spatial autocorrelation.

$$\log(LWC(Z, ZDR) = 0.058Z - 0.118ZDR - 2.36 \tag{2.5}$$

Equation 2.5 shows improved spatial coverage compared to all previous equations, with VIL in the high reflectivity region clearly visible (Fig. 10j). High reflectivity regions in both the eastern and the western cluster exhibit VIL values exceeding 0.4 kg/m^2. Additionally, there is an expanded region with VIL values ranging from 0.05 to 0.1 kg/m^2 as well and we can see this very distinctively. A small region in the northwest displays VIL values exceeding 0.4 kg/m^2, which was not visible in any of the previous estimations. Positive bias has been notably reduced across most areas, though some negative bias persists in low reflectivity regions (Fig. 10k). However, regions where observations indicate VIL values surpassing 0.3 kg/m^2 show a positive bias exceeding 0.2.

The highest STD of 0.029 for VIL from radar is calculated. The RMSD of 0.133 suggests discrepancies between observed and predicted values. The MBD of −0.090 suggests underestimation in VIL predictions, while the MAE of 0.105 reflects the average magnitude of prediction errors. Moreover, Eq. 2.5 exhibits a BMI of 0.8, indicating the

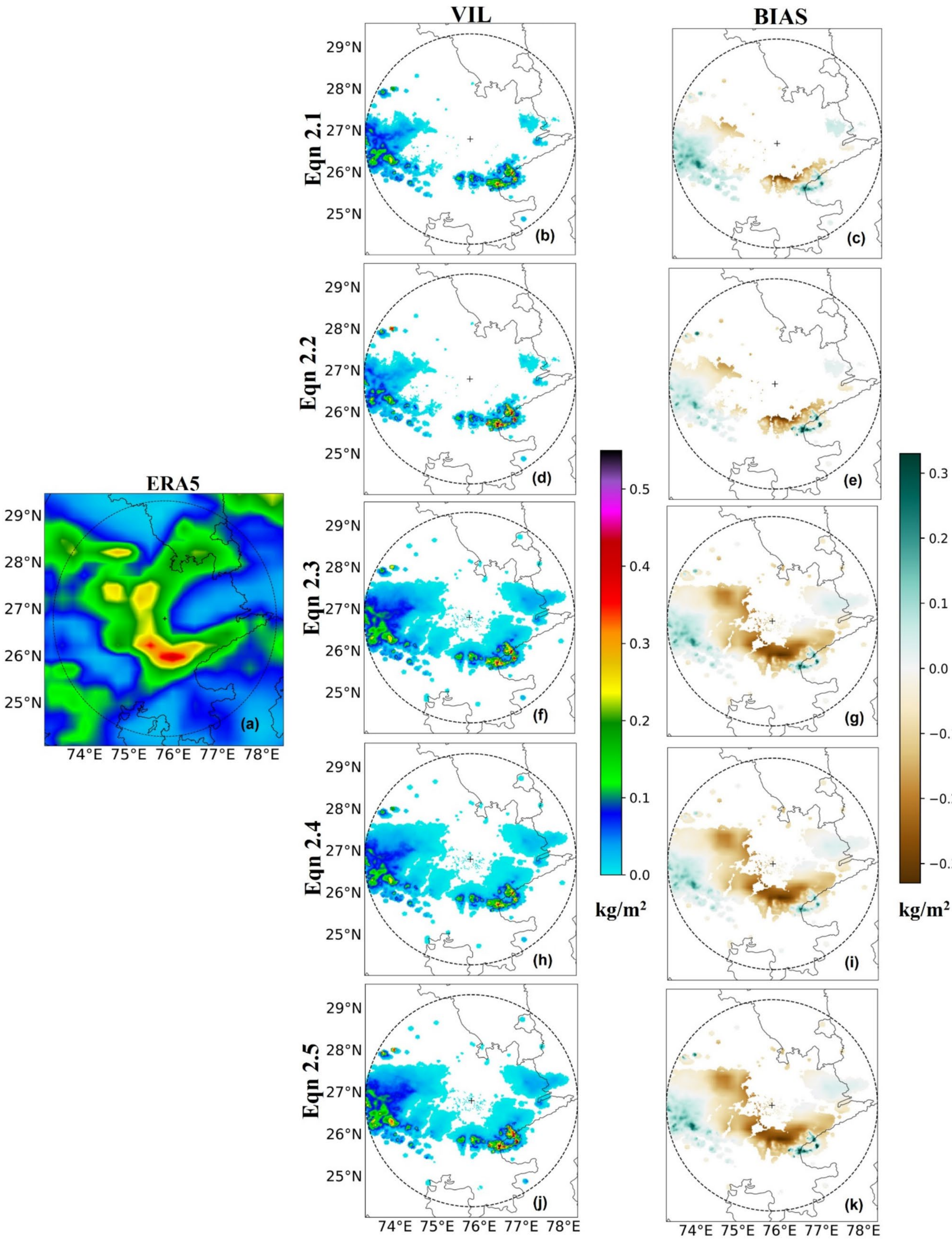
ERA5
VIL
BIAS
Eqn 2.1
Eqn 2.2
Eqn 2.3
Eqn 2.4
Eqn 2.5
29°N
28°N
27°N
26°N
25°N
74°E 75°E 76°E 77°E 78°E
(a)
(b)
(c)
(d)
(e)
(f)
(g)
(h)
(i)
(j)
(k)
0.5
0.4
0.3
0.2
0.1
0.0
kg/m²
0.3
0.2
0.1
0.0
−0.1
−0.2
−0.3
kg/m²

◂**Fig. 10** (**a**) Observed TCCLW(kg/m^2) from ERA-5, (**b** & **c**) radar estimated VIL using Eq. 2.1 and its bias respectively, (**d** & **e**) radar estimated VIL using Eq. 2.2 and its bias respectively,(**f** & **g**) radar estimated VIL using Eq. 2.3 and its bias respectively, (**h** & **i**) radar estimated VIL using Eq. 2.4 and its bias respectively and (**j** & **k**) radar estimated VIL using Eq. 2.5 and its bias respectively for 13:00UTC on 25 June 2020

strongest spatial autocorrelation in TCCLW values, emphasising the spatial coherence captured by the equation. The analysis of equations showcases promising advancements in estimating VIL from radar data. Equation 2.1 demonstrates a good performance across regions with lower error matrices. However, Eq. 2.5 excels in spatial coverage and spatial coherence, making it especially effective for capturing larger areas. While it introduces slightly more errors in high reflectivity zones, its advantages in broader coverage make it a strong contender**.** (Results for another event, 14:00 UTC of 1 July 2022, which also gave similar results are added in supplementary datasets, Figs. 1 and Table. s1).

3.2.2 Day analysis for 25 June 2020

Moving into daily analysis, Fig. 11 illustrates the radar-estimated VIL retrievals across different equations with observation and bias for 25 June 2020. The statistical analysis has been shown in Table 5 and standard deviation plots are given in Fig. 12.

The 24-h TCCLW (Fig. 11a) ranges up to 0.23 kg/m^2 within the radar range. The major spatial structure shows values between 0.1 and 0.2 kg/m^2 in the lower eastern and northeastern parts. Additionally, there are VIL regions with values below 0.05 kg/m^2 in the western part, where one of the major cloud clusters was identified from the maximum reflectivity plot (Fig. 8b). Another patch with similar values is in the central-southwestern part of the region, where a second cloud cluster is present. A similar pattern is observed in the northern part of the region as well. The remaining areas exhibit values ranging from 0.05 to 0.1 kg/m^2. The spatial standard deviation analysis (Fig. 12a) shows that regions with higher VIL values also have higher standard deviations (0.6–0.8), while the rest of the region has lower standard deviations.

Considering the VIL estimates using Eq. 2.1 (Fig. 11b), two clusters are visible on both the eastern and western sides with VIL values ranging from 0 to 0.5 kg/m^2 similar to observation (Fig. 11a). Small patches of VIL values in the same range are also observed in the northwestern part of the region. Analysing the bias of the estimation (Fig. 11c), regions with VIL values greater than 0.05 kg/m^2 exhibit a lower negative bias ranging from −0.06 to less than −0.02, indicating slight underestimation. A higher negative bias is noted in the low reflectivity region of the cluster, while the rest of the region shows either a lower negative bias (up to −0.1 or more) or near-zero biases. The STD plot for Eq. 2.1 (Fig. 12b) demonstrates that areas with higher VIL values also have higher STD values ranging from 1.2 to 1.4 or more, indicating significant variability in VIL values within the high reflectivity region and surrounding regions.

The VIL estimation using Eq. 2.2 (Fig. 11d) shows a spatial pattern similar to the observed data with VIL values ranging from 0.0 to 0.5 kg/m^2. The variation in spatial pattern compared to Eq. 2.1 (Fig. 11b) is minimal. Notably, the VIL values around the high VIL region of the western cluster are reduced to less than 0.05 kg/m^2, resulting in a less distinct pattern compared to Eq. 2.1 estimation, but it aligns more closely with the observation. This alignment is further reflected in the bias pattern (Fig. 11e), where the negative bias around the high reflectivity region approaches a low value. Additionally, in the STD plots (Fig. 12c), the areas where bias has moved towards zero also show a reduced STD of 0.4–0.6, indicating lower variability in these regions.

The VIL estimation using Eq. 2.3 (Fig. 11f) reveals a much clearer spatial pattern particularly around the boundaries of both clusters, especially in the western cluster with VIL values reaching 0.05 kg/m^2, similar to the observation (Fig. 10a). This improved clarity is also evident in the clustering of other smaller regions. When assessing with the bias (Fig. 10g), it is observed that these regions have negative bias values, ranging from −0.02 or lower. The STD plot (Fig. 11d) also indicates that regions with elevated VIL values also exhibit higher STD, exceeding 1.2, reflecting greater variability in these areas. The spatial pattern of VIL estimated using Eq. 2.4 (Fig. 11h) is less distinct compared to Eq. 2.3. While the spatial distribution of bias (Fig. 11i) shows negative bias around the high reflectivity region, similar to Eq. 2.3, these regions also exhibit higher STD, exceeding 1.2 (Fig. 12e). This suggests that despite the lower negative bias in the core areas, the variability in VIL values is relatively high.

Equation 2.5 offers a notably well-defined VIL estimation structure (Fig. 11j), surpassing the clarity seen in previous equations. This improved estimation is particularly evident in the western cluster of the region and aligns closely with the observed pattern (Fig. 11a), capturing the essence of both clusters effectively. There is an addition of a VIL region with values up to 0.05 kg/m^2 near the radar location, as well as a similar trend in the eastern part of the region. The bias analysis (Fig. 11k) highlights that while the newly added region shows a negative bias of −0.06 or lower, the high VIL region with VIL values greater than 0.05 kg/m^2 demonstrates a lower negative bias of less than −0.02. The STD (Fig. 12f) further reinforces these improvements, showing higher values (greater than 1.2) in the high reflectivity region and lower values in the surrounding areas.

Table 4 Table of error matrix showing the statistical analysis between ERA5 TCCLW (kg/m^2) and radar retrieved VIL (kg/m^2) for 13:00:00 UTC June 25 2020

Source	STD	RMSE	MBD	MAE
ERA5	0.072			
Equation 2.1	0.023	0.112	−0.068	0.085
Equation 2.2	0.024	0.115	−0.071	0.088
Equation 2.3	0.027	0.130	−0.090	0.103
Equation 2.4	0.023	0.133	−0.097	0.106
Equation 2.5	0.029	0.133	−0.090	0.105

In the 24-h analysis also we can see that regions with high reflectivity have higher VIL values and these are also the locations with low negative bias but with a high standard deviation. From the estimation of Eq. 2.5 we can see a better spatial clarity in the structures. Among the equations, Eq. 2.1 has the lowest STD of 0.024 but exhibits the highest RMSD of 0.138, indicating significant average prediction errors. It's very weak, r of 0.052 and MAE of 0.102 suggest lower accuracy and a tendency to underpredict. Equations 2.2 and 2.3 show low variability with STDs of 0.025 and 0.028, respectively. Both equations have moderate RMSD values (0.120 for 2.2 and 0.135 for 2.3) and weak correlations (r of 0.054 for 2.2 and 0.095 for 2.3), reflecting similar issues with prediction accuracy and moderate overall errors. Equation 2.4, with an STD of 0.027 and an RMSD of 0.137, also displays relatively low variability but moderate prediction errors and a weak correlation (r of 0.076). In comparison, Eq. 2.5 outperforms the others with an STD of 0.029, a moderate RMSD of 0.115, and a weak but positive correlation coefficient (r) of 0.079. Its MAE of 0.085 and MBD of −0.065 reflect a moderate level of overall error and a slight tendency to underpredict. Moreover, Eq. 2.5 achieves the highest BMI value of 0.04, indicating the strongest spatial autocorrelation among the models. (Result for another day, 1 July 2022 is added in supplementary datasets Figs. 2, s3 and Table s2).

3.2.3 Comparative analysis of radar derived VIL with other parameters on June 25, 2020

We utilised one swath of MODIS data, ERA5 precipitation type data and reflectivity to analyse the DWR-estimated VIL using Eq. 2.5, which was identified as the most accurate based on hourly and daily analysis.

A clear and well-defined pattern of liquid water is evident in the LWP retrieval from MODIS (Fig. 13a). A U-shaped structure extending from the northwestern part to the northeastern part is seen with VIL values ranging from 0.4 kg/m^2 and higher where the cluster present in the northern part values less than 0.4 kg/m^2 is present. In the southern region, we can see cloud structure with LWP values up to 0.5 kg/m^2 in and out of the radar range. Most of the other regions, including the central part have values less than 0.1 kg/m^2. DWR-estimated VIL (kg/m^2) (Fig. 13b) also shows a U-shaped structure in the northern part with similar values to that of the satellite-derived liquid water even though the size of the clusters is comparatively small. Conversely, it exhibits lower values, often less than 0.1 kg/m^2 away from these high VIL central regions. In the southern region DWR could not detect any VIL whereas in the central part, small patches are visible Additionally, when comparing with the cloud phase (Fig. 13c), the MODIS algorithm categorizes regions where liquid water values are less than 0.1 kg/m^2 in both satellite and DWR data as water clouds. In the northern U-shaped cluster, where liquid water values are higher, most regions are either in an undetermined phase or classified as ice clouds, with only some parts categorized as water clouds. The southern region where most of the liquid water values are till 0.45 kg/m^2 is in the water cloud region with very small points in the ice cloud phase. Where VIL was identified by both satellite observations and DWR, most of the regions with water clouds show rainfall according to precipitation type (Fig. 13d), indicating precipitation in liquid form. The region with higher liquid water also corresponds to high reflectivity (> 40 dBZ) and a maximum vertical height of over 10 km (Fig. 13e), resulting from a significant number of hydrometeors, including liquid water. Overall, the spatial pattern of radar-retrieved VIL closely matches the satellite observations, with values higher in the high reflectivity regions. Areas with detected liquid water align with regions identified as water clouds, and locations with rain are accurately categorised as precipitation type. However, the radar could not detect VIL in some regions, especially in the south, where satellites did. This discrepancy may be due to beam blockage. This may be because the DWR data come from weather radar, which might not be able to detect small liquid droplets. Interpolating MODIS data from 1 km resolution to 2 km to match radar resolution may not significantly affect the bias, though the satellite could provide more detailed data. However, the closest radar data is at 08:42 UTC, while the satellite data is at 08:45 UTC. This 3-min gap can influence the spatial spread of liquid water, as the cloud system may have grown during this time, although the impact is likely not significant as the development of cloud droplets into raindrops occurs on the order of ten minutes in convective clouds (Murty and Chandrasekhar 2011).

3.2.4 Daily analysis of selected days

For each selected day, RMSE and MAE have been calculated for the daily estimated VIL relative to ERA5 TCCLW. Figure 14 shows these error matrices along with area-weighted average rainfall.

Examining the error matrices for 2020 (Fig. 14a for RMSE and b for MAE), Eq. 2.5 consistently exhibited lower RMSE and MAE values across various days, demonstrating its superior accuracy in estimating rainfall. Specifically, RMSE values for Eq. 2.5 ranged from 0.061 to 0.102, while MAE values ranged from 0.056 to 0.155. These values are typically the lowest among the equations assessed. Equation 2.3 demonstrated competitive performance but generally had higher error metrics. While Eq. 2.3 performed comparably on some days, it exhibited higher RMSE and MAE values than Eq. 2.5 on several occasions, particularly during high-intensity rainfall events. The other equations (Eq. 2.1, Eq. 2.2, and Eq. 2.4) showed slightly higher RMSE and MAE values than to Eq. 2.5. Despite their initial strong performance during July, when the SW monsoon just arrived in the region with low rainfall intensity, they generally exhibited less accuracy in rainfall estimation relative to Eq. 2.5 later on. The analysis revealed that RMSE and MAE values increased with higher rainfall intensity. For instance, on high rainfall days such as August 20, 2020, with 455.51 mm of rainfall, the RMSE and MAE values were elevated, indicating that error metrics tend to increase with more intense rainfall events. However, Eq. 2.5 maintained relatively lower error metrics even on these high-intensity rainfall days, highlighting its robustness in handling varying rainfall conditions.

For 2021 (Fig. 13c for RMSE and d for MAE), in comparison, Eq. 2.1 shows slightly higher error metrics. The RMSE for Eq. 2.1 ranges from 0.053 to 0.374, while the MAE ranges from 0.049 to 0.272. These values are generally higher than those of Eq. 2.5, indicating a less accurate performance. Equation 2.2's performance is close to that of Eq. 2.1, but it still exhibits slightly higher error metrics compared to Eq. 2.5. Equation 2.3 displays competitive performance but tends to have higher RMSE and MAE values compared to Eq. 2.5 in several days. Similarly, Eq. 2.4 also has slightly higher error metrics than Eq. 2.5. Equation 2.5 consistently demonstrates lower RMSE and MAE values compared to other equations. Specifically, the RMSE values for Eq. 2.5 range from 0.051 to 0.373, while the MAE values range from 0.047 to 0.343. These lower values suggest that Eq. 2.5 provides more accurate VIL estimates. On several days, Eq. 2.5 achieved the lowest RMSE and MAE values, indicating superior accuracy, particularly for days with high-intensity rainfall. This superior performance highlights Eq. 2.5's effectiveness in accurately capturing VIL measurements, especially during significant rainfall events. Equation 2.5 consistently outperforms the other equations in terms of accuracy for estimating VIL, as indicated by its lower RMSE and MAE values.

For 2022 (Fig. 13e for RMSE and f for MAE), this also shows similar results, with Eq. 2.5 performing better. Equation 2.5 has lower MAE values compared to other equations. The RMSE values for Eq. 2.5 are generally lower, indicating better performance in terms of error magnitude. The other equations, Eq. 2.1 to Eq. 2.4, show higher MAE and RMSE values than Eq. 2.5 on many days. Specifically, Eq. 2.1 and Eq. 2.4 often have higher MAE and RMSE, indicating less accuracy in rainfall estimation. Although Eq. 2.2 and Eq. 2.3 perform well, Eq. 2.5 still outperforms them overall, with lower error metrics across the dataset. It also maintains lower errors even during high rainfall intensities, suggesting it handles high-intensity conditions more effectively. Even for lower rainfall conditions, such as on 19–06–2022 (168.69 mm), Eq. 2.5 maintains a lower error margin compared to others.

Overall, Eq. 2.5 consistently demonstrates superior accuracy in estimating rainfall across the selected days. Its lower RMSE and MAE values indicate it performs better than other equations, particularly during high-intensity rainfall events. While other equations like Eqs. 2.1, 2.2, 2.3, and 2.4 show competitive results, they generally exhibit higher error metrics compared to Eq. 2.5. This highlights Eq. 2.5's robustness and reliability in accurately capturing VIL measurements and handling varying rainfall conditions effectively. Overall, errors increase with increasing rainfall. The inclusion of ZDR in Eq. 2.5 enhances the estimation of liquid water content and VIL by accounting for the shape and distribution of hydrometeors, even in high rainfall situations**.** High errors during intense rainfall can be attributed to several interrelated factors. During heavy rainfall, anomalous propagation, occultation by large droplets during strong updrafts, beam-broadening effects with non-uniform beam filling, and attenuation and scattering contribute to increased errors in radar-based estimations. Additionally, assumptions about the drop size distribution (DSD) based on the Marshall-Palmer distribution may not hold, as drop size distributions deviate significantly from this model in intense rainfall conditions (Marshall and Palmer 1948; Harrison et al. 2000). Reflectivity is highly sensitive to the sixth power of droplet diameter (D^6) Doviak et al. (1994), which can lead to overestimation when larger drops dominate convective rain (Thomas et al. 2021). In contrast, during light rainfall, DSDs are more uniform, reducing such biases. ERA5, which relies on numerical weather prediction models to estimate liquid water content, may smooth out extreme values due to its coarser spatial and temporal resolution, leading to biases during heavy rainfall events. Moreover, intense precipitation often involves mixed-phase hydrometeors (e.g., rain, hail, graupel) and strong vertical motions, further complicating reflectivity-based retrievals. However, ZDR offers an advantage in distinguishing between different hydrometeor types and mitigating some of these uncertainties.

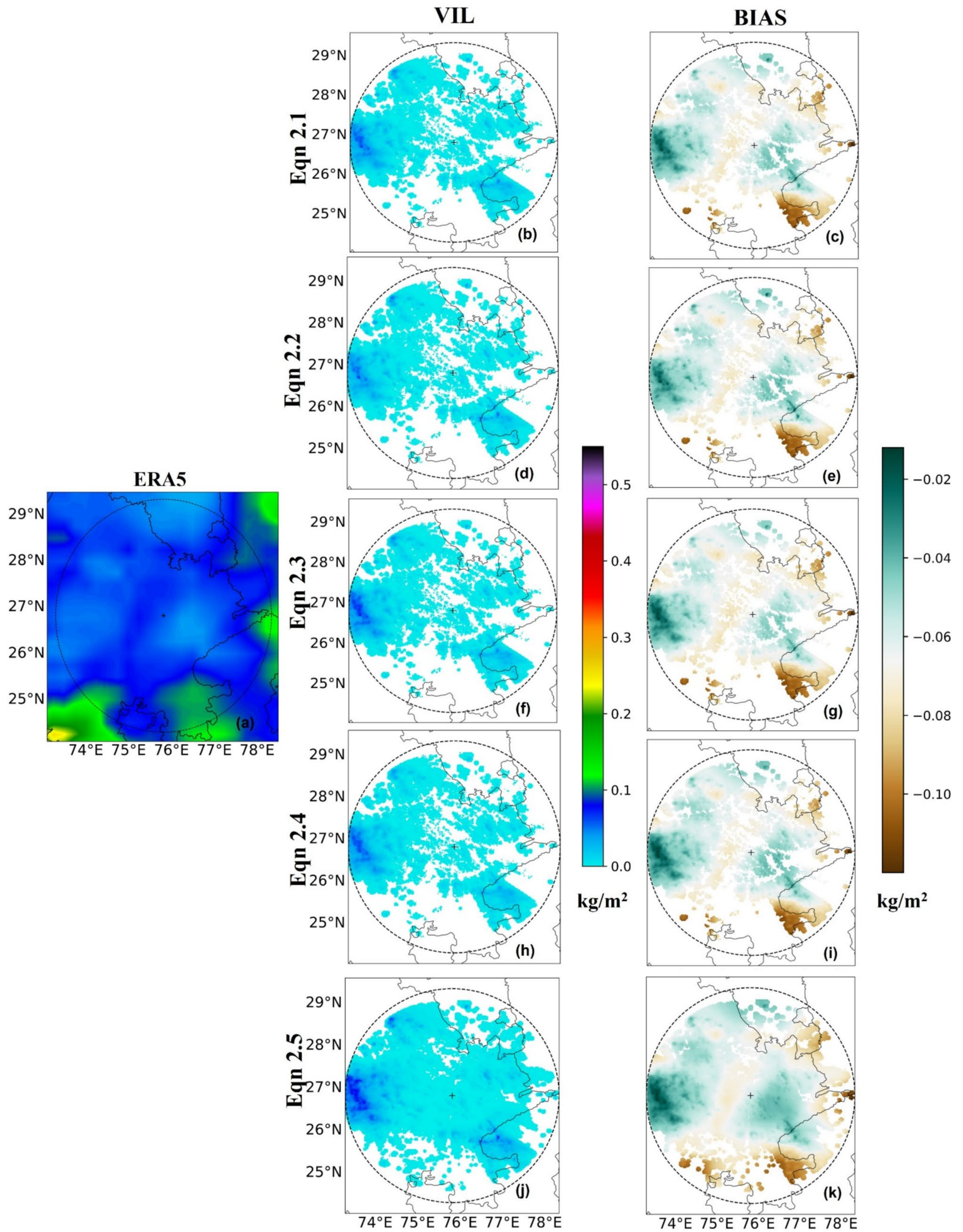
VIL
BIAS
ERA5
Eqn 2.1
Eqn 2.2
Eqn 2.3
Eqn 2.4
Eqn 2.5
29°N
28°N
27°N
26°N
25°N
74°E 75°E 76°E 77°E 78°E
(a)
(b)
(c)
(d)
(e)
(f)
(g)
(h)
(i)
(j)
(k)
0.5
0.4
0.3
0.2
0.1
0.0
kg/m²
−0.02
−0.04
−0.06
−0.08
−0.10
kg/m²

◂**Fig. 11** (**a**) Observed TCCLW(kg/m^2) from ERA-5, (**b** & **c**) radar estimated VIL using Eq. 2.1 and its bias respectively, (**d** & **e**) radar estimated VIL using Eq. 2.2 and its bias respectively, (**f** & **g**) radar estimated VIL using Eq. 2.3 and its bias respectively, (**h** & **i**) radar estimated VIL using Eq. 2.4 and its bias respectively and (**j** & **k**) radar estimated VIL using Eq. 2.5 and its bias respectively for 25 June 2020

Table 5 Table of error matrix showing the statistical analysis between ERA5 TCCLW (kg/m^2) and radar retrieved VIL (kg/m^2) for June 25 2020

Source	STD	RMSE	r	MBD	MAE
ERA5	0.072				
Equation 2.1	0.024	0.138	0.052	−0.068	0.102
Equation 2.2	0.025	0.120	0.054	−0.071	0.088
Equation 2.3	0.028	0.135	0.055	−0.090	0.103
Equation 2.4	0.027	0.137	0.076	−0.097	0.106
Equation 2.5	0.029	0.115	0.079	−0.065	0.085

4 Summary

To enhance precipitation forecasting and gain a deeper understanding of cloud processes, it is crucial to thoroughly investigate cloud microphysical parameters such as VIL across extensive spatial and temporal scales. In this study, VIL was estimated using four different sets of Z-LWC relationships and one Z, ZDR-LWC relationship collected from the literature, and the results were analysed for best performing one. For this, data from the C-Band DWR at the IMD Jaipur station for 78 SM heavy rainfall days in 2020, 2021, and 2022 were quality controlled, gridded and utilised. First, a long-term average study from 2003 to 2023 for LWCP and TCCLW, along with three different rainfall datasets, were analysed monthly and aggregated for the SM monsoon period. Further, VIL was estimated for 13:00 UTC, 25 June 2020 using all equations and was analysed relative to ERA5 TCCLW. Then VIL for the entire day was examined and VIL estimated from the best performing equation thus far was compared with parameters including MODIS-derived LWP and cloud phase for the time when satellite data was available for the day. Finally, VIL was estimated and analysed for all selected days for the best-performing equation overall.

A long-term study highlighted that liquid water is high in the southeastern part during June and spreads to the central and northern part by the next two months as the rainfall progresses. The value is lowest in June and September as

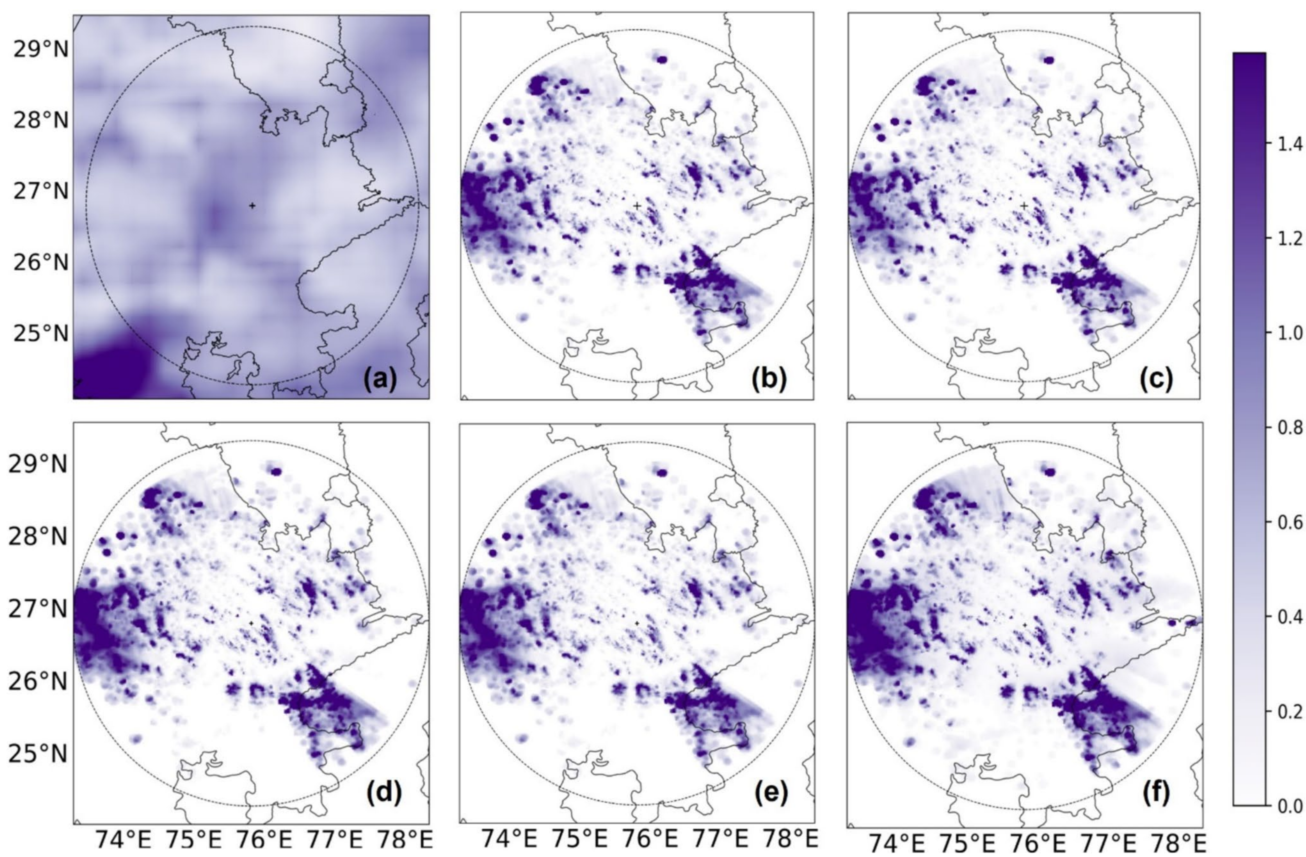

Fig. 12 Standard deviation plots of (**a**) ERA5 TCCLW, radar retrieved VIL using (**b**) Eq. 2.1, (**c**) Eq. 2.2, (**d**) Eq. 2.3, (**e**) Eq. 2.4 and (**f**) Eq. 2.5 for 25 June 2020

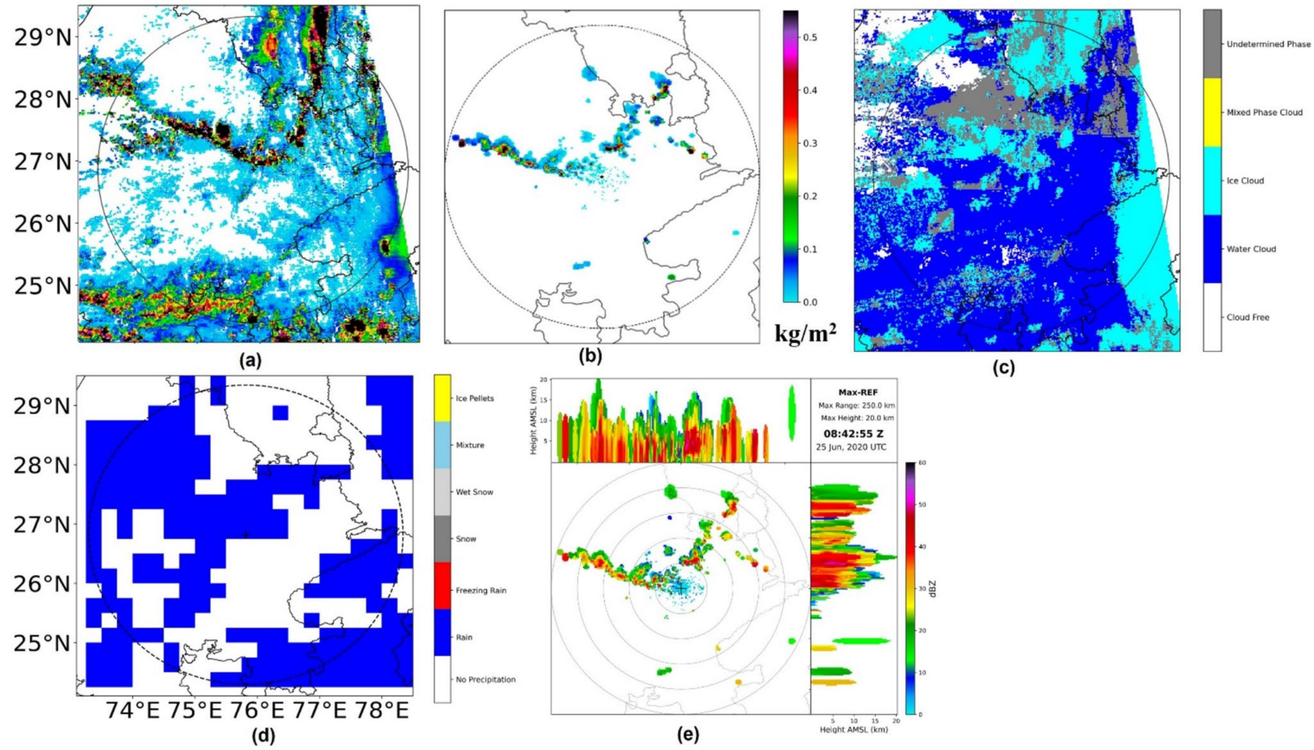

Fig. 13 Spatial distribution of (**a**) Liquid water path (kg/m^2) from MODIS at 08:45UTC, (**b**) VIL (kg/m^2) from DWR at 08:42UTC, (**c**) Cloud phase from MODIS at 08:45: 00 UTC, (**d**) Precipitation type from ERA5 for 09 00 UTC and (e) Max Reflectivity (dBZ) at 08:42: 00 UTC for 2020 June 25 over a region centering at DWR-Jaipur location (24N-30N; 73E-79E)

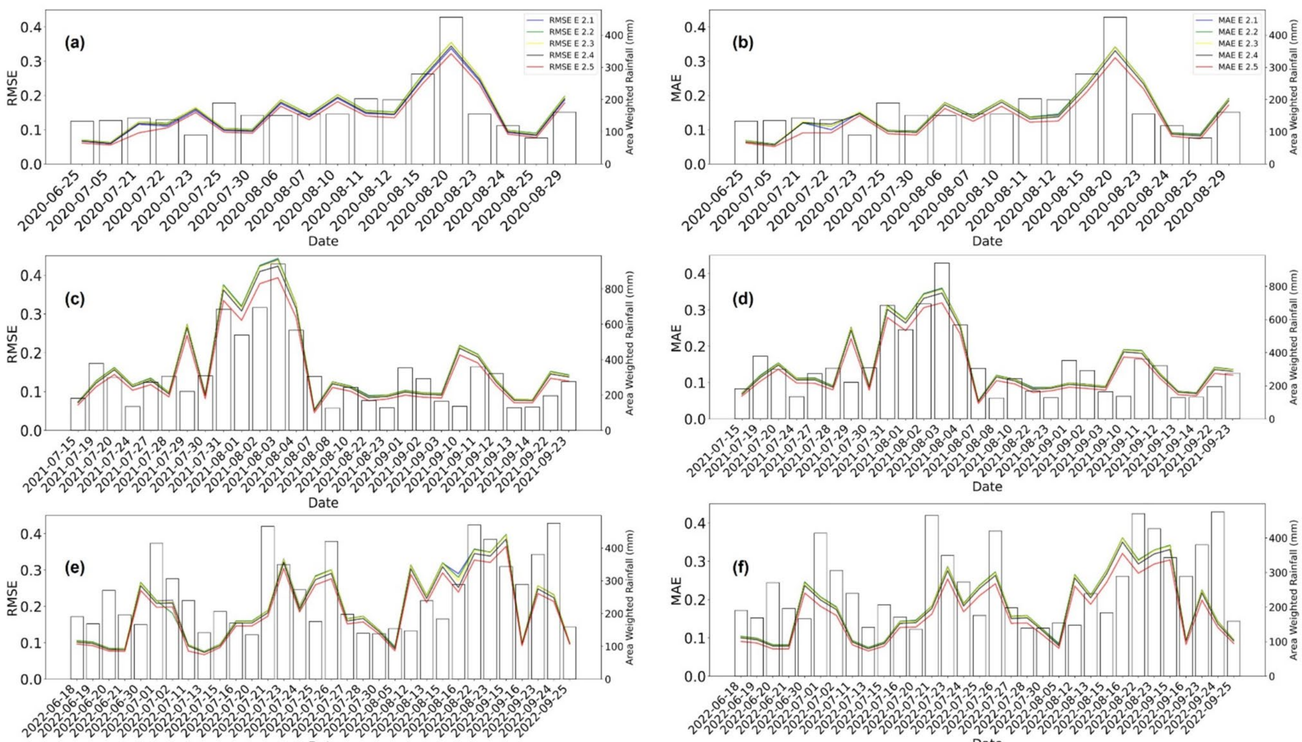

Fig. 14 Analysis of RMSE (left column) and MAE (right column) along with area weighted average rainfall (Bar plot) for the selected days for different equations during monsoon seasons of 2020 (**a**, **b**), 2021 (**c**, **d**) and 2022 (**e**, **f**)

it is the time when SM arrives and retreats. It showed a diagonal variation with higher values in the southeastern part and some concentration across the diagonal line probably because of the orographic effect of the Aravali range. Overall, there is good agreement between the observed and estimated values and locations. Radar-derived VIL shows the small-scale variation more accurately with high VIL in the high reflectivity region, clearly depicting the in-cloud variation of liquid water. During the mature stage, the higher VIL was observed in high reflectivity regions with positive bias, while lower VIL was found in lower reflectivity regions with negative bias. Nonetheless, Eq. 2.5, which incorporates ZDR data, significantly enhances VIL estimation by accurately detecting high VIL regions and reducing biases. We found that most locations where VIL was estimated by DWR and satellite corresponded to areas with liquid-phase clouds and rainfall, suggesting that VIL estimates are effective in identifying regions with active precipitation and significant liquid water content. In the daily analysis the result was interesting as there was no positive bias but with very low negative bias indicating slight underestimation. Bias was lower in high VIL regions with high STD. Despite a higher STD, Eq. 2.5 remains the most effective estimator. In the daily analysis of all selected days high error was seen on high rainfall days. Although all the equations yielded similar error estimations Eq. 2.5 considering hydrometeor shape and distribution consistently demonstrates superior accuracy with lower RMSE and MAE values particularly during high-intensity rainfall events. We also tested a sixth equation with Eq. 2.5's coefficients adjusted for the German DSD, but this equation led to extensive errors and did not improve quality.

This study is the first to comprehensively evaluate and compare multiple equations for estimating VIL using DWR data over the Indian domain. The insights gained into the strengths and limitations of each method will guide future studies in selecting and refining estimation techniques. The datasets retrieved by this way can be assimilated in real time, research-based studies and understanding the microphysical representation in the existing weather models. We saw that there are some areas where VIL shows ice clouds or undetermined phases. This can be addressed by developing VIL estimators for different convective systems such as deep and shallow convection. Data loss by beam blockage can be addressed by optimized radar scanning strategies (adjusting elevation angles), terrain-based corrections for radar derived variables, multi-radar or multi-sensor fusion (combining data from other radars or satellites). Additionally, incorporating in situ measurements such as disdrometer into the analysis can address the shifts observed in the location of some VIL clusters probably resulted by interpolation of ERA5 data and assist in developing region and cloud-type estimators. Including ZDR improves applicability across regions and seasons by providing hydrometeor shape and size information. This enhances accuracy in mixed-phase precipitation and non-uniform drop size distributions while reducing errors by distinguishing hail from large raindrops. Further other polarimetric variables like KDP and correlation coefficient (ρhv) in conjunction with ZDR and methods such as attenuation-based estimation can be done. Relying solely on C-band radar can underestimate VIL, integrating multi-frequency radar (e.g., Ka or W) and satellite data may enhance sensitivity and accuracy. This study is among the first to thoroughly evaluate and compare multiple equations for estimating VIL using DWR data in the Indian region. The insights gained will serve as a valuable reference for future research, helping to refine and adopt more appropriate estimation techniques. The datasets generated in this study can be integrated into real-time simulations, which the authors will explore in future steps to enhance the representation of cloud microphysics in current weather models.

Supplementary Information The online version contains supplementary material available at https://doi.org/10.1007/s00704-025-05454-7.

Acknowledgements I would like to acknowledge India Meteorological Department (IMD) for providing Doppler Weather Radar and the work is supported by MoES project(MOES/16/02/2021-RDESS/NARM-2) sponsored by the Ministry of Earth Sciences, Government of India.

Author contributions Albin Sabu analyse and prepared the manuscript, Hamid Shayed Ali process the DWR data, Gargi Rakshit -satellite analysis, S.K. Panda, Someshwar Das and Devesh Sharma—Conceptulization, Review and Suggestions, Jayanti pal-Conceptulization, review, editing.

Funding Funded by Ministry of Earth Sciences (MoES), Government of India, New Delhi, under NARM mission (Ref:MOES/16/02/2021-RDESS/NARM-2).

Data availability No datasets were generated or analysed during the current study.

Declarations

Ethics approval Not applicable.

Consent to participate Not applicable.

Consent to publish Not applicable.

Competing interests The authors declare no competing interests.

References

Adler RF, Huffman GJ, Chang A, Ferraro R, Xie P, Janowiak J, Rudolf B, Schneider U, Curtis S, Bolvin D, Gruber A, Susskind J, Arkin P (2003) The version 2 Global Precipitation Climatology Project (GPCP) monthly precipitation analysis (1979-Present). J Hydrometeor 4:1147–1167

ALI M, Joardar D, Loe BR (2005) Variability of southwest monsoon over Rajasthan and Kerala. Mausam, 56(3), 593–600. https://doi.org/10.54302/mausam.v56i3.989

Amburn SA, Wolf PL (1997) VIL density as a hail indicator. Weather Forecast 12(3):473–478

Angulo-Martínez M, Beguería S, Latorre B, Fernández-Raga M (2018) Comparison of precipitation measurements by OTT Parsivel 2 and Thies LPM optical disdrometers. Hydrol Earth Syst Sci 22(5):2811–2837

Aydin K, Singh J (2004) Cloud ice crystal classification using a 95-GHz polarimetric radar. J Atmos Oceanic Tech 21(12):1679–1688

Barnes SL (1964) A technique for maximizing details in numerical weather map analysis. J Appl Meteorol 3(4):396–409. https://doi.org/10.1175/1520-0450(1964)003%3c0396%3e2.0.CO;2

Bodas-Salcedo A, Mulcahy JP, Andrews T, Williams KD, Ringer MA, Field PR, Elsaesser GS (2019) Strong dependence of atmospheric feedbacks on mixed-phase microphysics and aerosol-cloud interactions in HadGEM3. J Adv Model Earth Syst 11(6):1735–1758

Bringi VN, Chandrasekar V (2001) Polarimetric Doppler Weather Radar, Cambridge University Press, Cambridge. https://doi.org/10.1017/CBO9780511541094

Carlin JT, Ryzhkov AV, Snyder JC, Khain A (2016) Hydrometeor mixing ratio retrievals for storm-scale radar data assimilation: utility of current relations and potential benefits of polarimetry. Mon Weather Rev 144(8):2981–3001. https://doi.org/10.1175/MWR-D-15-0423.1

Cifelli R, Nesbitt SW, Rutledge SA, Petersen WA, Yuter S (2007) Radar characteristics of precipitation features in the EPIC and TEPPS regions of the east Pacific. Mon Weather Rev 135(4):1576–1595

Doviak RJ, Zrnic DS, Schotland RM (1994) Doppler radar and weather observations. Applied Optics 33(21):4531

Fovell RG, Su H (2007) Impact of cloud microphysics on hurricane track forecasts. Geophys Res Lett 34:L24810

Frech M, Hubbert J (2020) Monitoring the differential reflectivity and receiver calibration of the German polarimetric weather radar network. Atmos Meas Tech 13:1051–1069. https://doi.org/10.5194/amt-13-1051-2020

Gabella M, Notar Pietro R (2002) ERAD 2002 Ground clutter characterization and elimination in mountainous terrain. In: Proceedings of ERAD, pp 305–311

Gascón E, Sánchez JL, Fernández-González S, Hermida L, López L, García-Ortega E, Merino A (2015) Monitoring a convective winter episode of the Iberian Peninsula using a multichannel microwave radiometer. J Geophys Res: Atmospheres 120(4):1565–1581

Georgakakos KP (2000) Covariance propagation and updating in the context of real-time radar data assimilation by quantitative precipitation forecast models. J Hydrol 239(1–4):115–129

George JP, Johny CJ, Raghavendra A (2011) DWR data monitoring and processing at NCMRWF. NMRF/TR/03/2011

Greene DR, Clark RA (1972) Vertically integrated liquid water – a new analysis tool. Mon Wea Rev 100:548–552. https://doi.org/10.1175/1520-0493(1972)1002.3.CO;2

Harrison DL, Driscoll SJ, Kitchen M (2000) Improving precipitation estimates from weather radar using quality control and correction techniques. Meteorol Appl 7:135–144

Heistermann M, Jacobi S, Pfaff T (2013) Technical note: an open source library for processing weather radar data (wradlib). Hydrol Earth Syst Sci 17(2):863–871. https://doi.org/10.5194/hess-17-863-2013

Helmus JJ, Collis SM (2016) The python ARM radar toolkit (Py-ART), a library for working with weather radar data in the python programming language. J Open Res Softw 4(1):25. https://doi.org/10.5334/jors.119

Hersbach H, Bell B, Berrisford P, Hirahara S, Horányi A, Muñoz-Sabater J, Nicolas J, Peubey C, Radu R, Schepers D, Simmons A, Soci C, Abdalla S, Abellan X, Balsamo G, Bechtold P, Biavati G, Bidlot, et al (2020) The ERA5 global reanalysis. Q J R Meteorol Soc 146(730):1999–2049. https://doi.org/10.1002/qj.3803

Hirano K, Maki M (2010) Method of VIL calculation for X-band polarimetric radar and potential of VIL for nowcasting of localized severe rainfall-Case study of the Zoshigaya downpour, 5 August 2008. Sola 6:89–92

Huffman G, Bolvin D, Braithwaite D, Hsu K, Joyce R, Xie P (2014) Integrated Multi-satellitE Retrievals for GPM (IMERG), version 4.4. NASA's Precipitation Processing Center. ftp://arthurhou.pps.eosdis.nasa.gov/gpmdata/. Accessed 31 Mar 2015

Illingworth AJ, Blackman TM, Goddard JW (2000) Improved rainfall estimates in convective storms using polarisation diversity radar. Hydrol Earth Syst Sci 4(4):555–563

Islam R, Rasmussen P (2008) Improved high resolution radar based rainfall estimation. J Hydrol Eng 13:910–913. https://doi.org/10.1061/(ASCE)1084-0699(2008)13:9(910)

Jacobi S, Heistermann M (2016) Benchmarking attenuation correction procedures for six years of single-polarised c-band weather radar observations in south-west germany. Geomat Nat Haz Risk. https://doi.org/10.1080/19475705.2016.1155080

Johansson E, Devasthale A, L'Ecuyer T, Ekman AM (2015) L, and Tjernström, M (2015) The vertical structure of cloud radiative heating over the Indian subcontinent during summer monsoon. Atmos Chem Phys 15:11557–11570. https://doi.org/10.5194/acp-15-11557-2015

Kraemer S, Verworn HR (2008) 11th International Conference on Urban Drainage, Edinburgh, Scotland, UK, 2008 Improved C-band radar data processing for real time control of urban drainage systems

Kumar A, Singh N, Singh A (2019) Observations on the distribution of clouds over northern India using joint CloudSat and CALIPSO measurements. Remote Sensing Letters, 10(6), 590–597. https://doi.org/10.1080/2150704X.2019.1587198

Lai A, Min J, Gao J, Ma H, Cui C, Xiao Y, Wang Z (2020) Assimilation of radar data, pseudo water vapor, and potential temperature in a 3DVAR framework for improving precipitation forecast of severe weather events. Atmosphere 11(2):182

Lee S-I (2001) Developing a bivariate spatial association measure: an integration of Pearson's r and Moran's I. J Geogr Syst 3:369–385

Li R, Guo J, Fu Y, Min Q, Wang Y, Gao X, Dong X (2015) Estimating the vertical profiles of cloud water content in warm rain clouds. J Geophys Res: Atmospheres 120(19):10–250

Liou KN, Ou SC (1989) The role of cloud microphysical processes in climate: an assessment from a one-dimensional perspective. J Geophys Res: Atmospheres 94(D6):8599–8607

Lyras NK, Kourogiorgas CI, Panagopoulos AD (2017) Optical satellite links channel modeling: time series generator and mitigation techniques evaluation. In: 2017 11th European Conference on Antennas and Propagation (EUCAP). IEEE, pp 50–53

Marshall JS, Palmer WMK (1948) The distribution of raindrops with size. J Meteorol 5:165–166. https://doi.org/10.1175/1520-0469(1948)005%3c0165:tdorws%3e2.0.co;2

Matrosov SY (2009) A method to estimate vertically integrated amounts of cloud ice and liquid and mean rain rate in stratiform precipitation from radar and auxiliary data. J Appl Meteorol Climatol 48(7):1398–1410

Mohan PR, Srinivas CV, Yesubabu V, Others. (2024) Evaluation of WRF cloud microphysics schemes in explicit simulations of Tropical Cyclone 'Fani' using wind profiler radar and multi-satellite data products. Pure Appl Geophys 181:2317–2341. https://doi.org/10.1007/s00024-024-03517-w

Moran KP, Martner BE, Post MJ, Kropfli RA, Welsh DC, Widener KB (1998) An unattended cloud-profiling radar for use in climate research. Bull Am Meteor Soc 79(3):443–456

Murty TS, Chandrasekhar A (2011) Basics pf atmospheric science. Nat Hazards 56:403–405. https://doi.org/10.1007/s11069-010-9590-x

Nesbitt SW, Cifelli R, Rutledge SA (2006) Storm morphology and rainfall characteristics of TRMM precipitation features. Mon Wea Rev 134:2702–2721

Pai DS, Sridhar L, Rajeevan M, Sreejith OP, Satbhai NS, Mukhopadhyay B (2014) Development of a new high spatial resolution (0.25° × 0.25°) long period (1901–2010) daily gridded rainfall data set over India and its comparison with existing data sets over the region. MAUSAM 65(1):1–18

Pattnaik S, Inglish C, Krishnamurti T (2011) Influence of rain-rate initialization, cloud microphysics, and cloud torques on hurricane intensity. Mon Weather Rev 139:627–649. https://doi.org/10.1175/2010MWR3382.1

Pinsky M, Khain A (2018) Theoretical analysis of the entrainment–mixing process at cloud boundaries. Part I: droplet size distributions and humidity within the interface zone. J Atmos Sci 75(6):2049–2064

Platnick S, Meyer KG, King MD, Wind G, Amarasinghe N, Marchant B, Arnold GT, Zhang Z, Hubanks PA, Holz RE, Yang P, Ridgway WL, Riedi J (2017) The MODIS cloud optical and microphysical products: collection 6 updates and examples from Terra and Aqua. IEEE Trans Geosci Remote Sens 55(1):502–525. https://doi.org/10.1109/TGRS.2016.2610522

Rajeevan M, Rohini P, Niranjan Kumar K, Srinivasan J, Unnikrishnan CK (2013) A study of vertical cloud structure of the Indian summer monsoon using CloudSat data. Clim Dyn 40:637–650

Randall D, Khairoutdinov M, Arakawa A, Grabowski W (2003) Breaking the cloud parameterization deadlock. Bull Am Meteor Soc 84:1547–1564. https://doi.org/10.1175/bams-84-11-1547

Rinehart RE (2004) Radar for meteorologists 4th edn. Rinehart Publications, Columbia, Mo p 482

Roh W, Satoh M, Hagihara Y, Horie H, Ohno Y, Kubota T (2024) An evaluation of microphysics in a numerical model using Doppler velocity measured by ground-based radar for application to the EarthCARE satellite. Atmos Meas Tech 17(11):3455–3466

Roy AB, Jakhar SR (2002) Geology of Rajasthan (Northwest India) Precambrian to Recent. Scientific Publishers (India), Jodhpur, pp 1–421

Saunders PE (2018) Objective identification and tracking of ZDR columns in x-band radar observations (M.S. Thesis) [Dept of Earth, Atmosphere, and Planetary Sciences]. Purdue University. West Lafayette, IN. https://docs.lib.purdue.edu/open_access_theses/1452/

Schulte RM, Lebsock MD, Haynes JM, Hu Y (2024) A random forest algorithm for the prediction of cloud liquid water content from combined CloudSat–CALIPSO observations. Atmos Meas Tech 17(11):3583–3596

Seliga TA, Bringi VN (1976) Potential use of radar differential reflectivity measurements at orthogonal polarizations for measuring precipitation. J Appl Meteorol 15:69–76. https://doi.org/10.1175/15200450(1976)015%3c0069:PUORDR%3e2.0.CO;2

Seo BC, Krajewski WF, Qi Y (2020) Utility of vertically integrated liquid water content for radar-rainfall estimation: quality control and precipitation type classification. Atmos Res 236:104800

Skripniková K, Řezáčová D (2014) Radar-based hail detection. Atmos Res 144:175–185

Stephens GL, O'Brien D, Webster PJ, Pilewski P, Kato S, Li JL (2015) The albedo of Earth. Rev Geophys 53(1):141–163

Syed HA, Sayyed I, Kalapureddy MCR, Grandhi KK (2024) PyScanCf – The library for single sweep datasets of IMD weather radars.https://doi.org/10.5281/ZENODO.10695154

Tapiador FJ, Navarro A, Levizzani V, García-Ortega E, Huffman GJ et al (2017) Global precipitation measurements for validating climate models. Atmos Res 197:1–20

Thomas A, Kanawade VP, Chakravarty K, Srivastava AK (2021) Characterization of raindrop size distributions and its response to cloud microphysical properties. Atmos Res 249:105292

Wang Z, Luo J, Li H, Zhu Y, He R (2024) The Direct Assimilation of Radar Reflectivity Data with a Two-Moment Microphysics Scheme for a Landfalling Typhoon in an OSSE Framework. Remote Sensing 16(22):4286. https://doi.org/10.3390/rs16224286

Widener KB, Mead JB (2004) W-Band ARM cloud radar – specifications and design. Fourteenth ARM science team meeting proceedings, Albuquerque, New Mexico, March 22–26

Witt A, Eilts MD, Stumpf GJ, Johnson JT, Mitchell EDW, Thomas KW (1998) An enhanced hail detection algorithm for the WSR-88D. Weather Forecast 13(2):286–303

Yang Y, Chen X, Qi Y (2013) Classification of convective/stratiform echoes in radar reflectivity observations using a fuzzy logic algorithm. J Geophys Res: Atmospheres 118(4):1896–1905

Yang Z, Liu P, Yang Y (2019) Convective/stratiform precipitation classification using ground-based Doppler radar data based on the K-nearest neighbor algorithm. Remote Sensing 11(19):2277

Yang S, Li D, Huang X, Liu Z, Pan X, Duan Y (2024) Assimilation of radar reflectivity via a full-hydrometeor assimilation scheme based on the WSM6 microphysics scheme in WRF 4D-Var. Mon Weather Rev 152(6):1303–1320. https://doi.org/10.1175/MWR-D-23-0137.1

Yum SS, Oh S-N, Kim J-Y, Kim C-K, Nam J-C (2004) Measurements of cloud droplet size spectra using a forward scattering spectrometer probe (FSSP) in the Korean Peninsula. J Korean Meteorol Soc 40(6):623–631 ((**In Korean**))

Zhang W, Xu G, Xi B, Ren J, Wan X, Zhou L, Cui C, Wu D (2020) Comparative study of cloud liquid water and rain liquid water obtained from microwave radiometer and micro rain radar observations over Central China during the monsoon. J Geophys Res: Atmospheres. https://doi.org/10.1029/2020JD032456

Zheng X, Tan W, Xu W, Huang P (2019) Vertically integrated liquid water analysis based on weather radar multisource data fusion. In: 2019 6th Asia-Pacific Conference on Synthetic Aperture Radar (APSAR). IEEE, pp 1–4

Zhong L, Liu L, Feng S, Ge R, Zhang Z (2011) A 35-GHz polarimetric Doppler radar and its application for observing clouds associated with typhoon Nuri. Adv Atmos Sci 28(5):945–956